

Biosensing with Insect Odorant-Receptor Functionalised Carbon Nanotube Devices

Introduction

So far in this thesis, multiple design schemes have been described for the construction of biosensors with insect odorant receptors. In ?@sec-fabrication, transducers were fabricated and characterised which used either graphene or various carbon nanotube network morphologies for the conductive channel. These morphologies included highly bundled networks from dropcasting in an organic solution, and less bundled networks dropcast in surfactant solution either with or without steam present. Functionalisation approaches using the attachment linkers PBASE, PBA/EDC, pyrene-NTA and pyrene-biotin were discussed in ?@sec-noncovalent-functionalisation, where linker functionalisation was investigated using electrical, spectroscopic and optical analysis techniques, including Raman spectroscopy and fluorescence microscopy. This investigation included a comparison of positive and negative aspects of each approach for their application in an iOR biosensor setting. The next step in the process was to integrate these components into a biosensor for testing in the redesigned vapour delivery system, as described in ?@sec-vapour-sensing-biosensors. In the vapour delivery system, signal responses can be compared to those measured by the non-selective onboard reference sensors. However, it was important to first ensure the functionalised devices worked consistently as biosensors in the existing aqueous sensing setup, as described in ?@sec-pristine-characteristics.

In the following chapter, aqueous sensing with insect odorant receptors was achieved with two different sensor functionalisation approaches, one where linker was attached to the transducer in organic solvent, and one where linker was preattached to odorant receptors and the process was performed entirely in aqueous solution. The first approach was more similar to those used previously for insect odorant receptor functionalisation [@Murugathas2019b; @Murugathas2020], but was not reproducible in a manner consistent enough for reliable testing with the vapour delivery system. A range of slight changes to this organic solvent functionalisation procedure were trialled to identify the source of the inconsistency in biosensor behaviour. The testing indicated that either surface coatings present on the device channels or the protective structure of the nanodiscs used were causing the quality of functionalisation to vary. The second approach, which eliminates both surface coatings and the nanodisc format, was therefore tested in the vapour delivery system. However, little response was shown by the functionalised sensor to the positive analyte. Finally, possible reasons for this lack of response are discussed.

Aqueous Sensing of Ethyl Hexanoate with OR22a-functionalised Carbon Nanotube Transistor

OR Nanodisc Functionalisation

A carbon nanotube network field-effect transistor device, fabricated using post-June 2023 methods as described in [?@sec-fabrication](#), was functionalised with OR22a nanodiscs. The network used for the device was deposited using the steam-assisted surfactant method, and the device was encapsulated with AZ® 1518 using the post-Jan 2023 photolithography mask. The functionalisation was performed as follows:

1. The device was exposed to UV light for 1 minute, placed in AZ® 326 developer for 3 minutes, then rinsed with acetone, isopropanol and nitrogen dried.
2. The device was vacuum annealed for 1 hour at 150°C.

Note: Steps 1 & 2 were added to ensure any residual photoresist on the channel was removed or passivated before functionalisation, see [?@sec-photoresist-contamination](#).

3. A solution of 1 mM PBASE (Setareh Biotech) in methanol was prepared by fully dissolving 2 mg PBASE in 5 mL methanol by vortex mixing at 1000 rpm in a dark room.

Note: PBASE was stored at -18°C for 18 months prior to use, and was thawed under vacuum for 15 minutes in dark conditions before opening.

4. The device was then rinsed with methanol, fully submerged in ~ 1 mL of PBASE in methanol solution and left covered with parafilm for 1 hour, then rinsed with methanol for 15 s, rinsed with 1× PBS for 15 s and nitrogen dried to remove residual PBASE.
5. The device was left dry and in darkness while collecting the OR22a nanodiscs from the -80°C freezer.
6. 10 µL OR22a nanodiscs (batch number ND-OR22a-SB018, 1.9 mg/mL, prepared 7 months earlier) were diluted in 1 mL freshly-prepared 1× PBS.

Note: The full 1 mL was used to flush out the nanodisc vial when preparing the nanodisc solution, with successive additions and subtractions of 50 µL 1× PBS into and from the vial.

7. The device was submerged in the OR22a nanodisc solution and left covered with parafilm for 1 hour, then rinsed with 1× PBS for 15 s and gently nitrogen dried.

The liquid-gated electrical characteristics shown in Figure 1 were taken using the B1500A semiconductor device analyser of the sensing channel (channel 7) before and after functionalisation with OR22a nanodiscs. The liquid-gate buffer used was 1× PBS containing 0.5% v/v

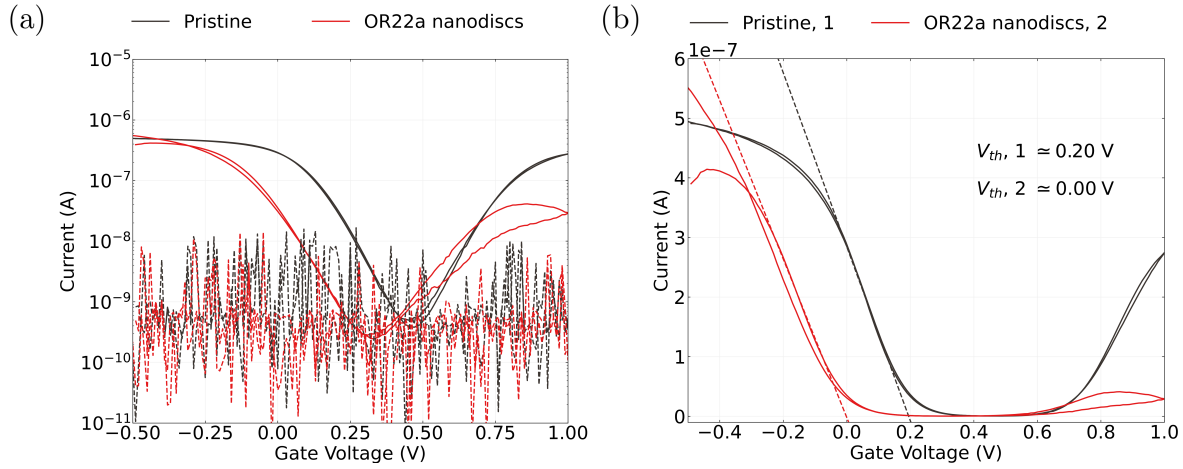


Figure 1: Liquid-gated carbon nanotube network device transfer characteristics before and after OR22a nanodisc functionalisation. Source-drain current was $V_{ds} = 100$ mV for both the forward and reverse sweep. In (a), the characteristics are shown on a logarithmic scale, where the gate current for each transfer curve is shown with a dashed line. In (b), the characteristics are shown on a linear scale alongside a dashed line tangent to the subthreshold slope of the characteristic curve. The threshold voltage corresponding to the intercept of this slope with the x-axis is shown for each transfer characteristic curve.

DMSO. The device exhibited ambipolar characteristics before functionalisation, which is typically seen for steam-deposited carbon nanotube films ([?@sec-electrical-characterisation-CNT](#); [?@sec-cnt-devices](#)). However, *p*-type behaviour dominates after device functionalisation due to a significant drop in *n*-type conductance. A slight increase in hysteresis was observed post-functionalisation. Leakage current (shown by the dashed traces) never exceeded 1×10^{-7} V, both before and after functionalisation. The significant change in electrical characteristics could be due to five possible factors — adsorption of solvent onto the network, network attachment of PBASE without subsequent protein attachment, non-specific adsorption of protein onto the network, PBASE-mediated attachment of the membrane scaffold protein (MSP) of nanodiscs to the network, and PBASE-mediated attachment of odorant receptors to the network. As the nanodisc volume is much larger than that of the odorant receptor, any direct protein adsorption most likely adsorption of the nanodisc membrane onto the carbon nanotube network. Odorant receptor attachment with PBASE is therefore the only desirable functionalisation result for sensing purposes. Functionalisation of the channel resulted in a negative shift in threshold voltage of -0.20 ± 0.03 V. This significantly exceeds the threshold voltage shifts measured for both methanol adsorption (-0.15 ± 0.02 V) and device exposure to PBASE in methanol (-0.06 ± 0.04 V), confirming that protein has attached to the carbon nanotubes. However, both direct protein adsorption [[@Bradley2004](#); [@Heller2008](#); [@Kauffman2008](#)] and empty nanodisc membrane attachment [[@Murugathas2019b](#)] should also lead to a significant negative threshold voltage shift and therefore increased *p*-conduction in the liquid-gated transfer characteristic curve. In all three cases, the voltage shift is predominantly the result of negative charge transfer from the adsorbed proteins to the semiconducting carbon nanotubes [[@Bradley2004](#); [@Heller2008](#); [@Murugathas2019b](#)]. It is likely that the negative shift observed results from some combination of the three types of attachment. It should be noted that while the size of the functionalisation-induced threshold voltage shift can be used to determine whether an amine-tagged protein has attached to the nanodisc network, it cannot be used to specifically determine whether odorant receptors have attached to the network.

Atomic force microscope images were taken of the device channels both before functionalisation and after sensing with the functionalised device to confirm the presence of nanodiscs. As far as the author knows, these are the first atomic force microscope images taken of iOR nanodiscs found on a sensing channel rather than on a separate carbon nanotube film; this was made possible by using the 20 μm wide aperture encapsulation mask discussed in [?@sec-encapsulation](#). AFM images showing iOR-nanodisc functionalised carbon nanotube networks have been reported by Murugathas *et al.*, but these images were not of channels used for sensing [[@Murugathas2019b](#)]. These images are shown in Figure 2. The visible features are much smaller than the agglomerated nanodisc features in the atomic microscope images taken by Murugathas *et al.* [[@Murugathas2019b](#)]. On the dense network morphology used here, the position of nanodisc clusters relative to the carbon nanotubes is also less distinct. To confirm whether nanodiscs have preferentially attached to the carbon nanotubes, a more quantitative approach is required.

Since no trough-like artifacts are visible in either the pristine or functionalised atomic force microscope images in Figure 2, a value of 1.8 nm was used as the mean substrate height for

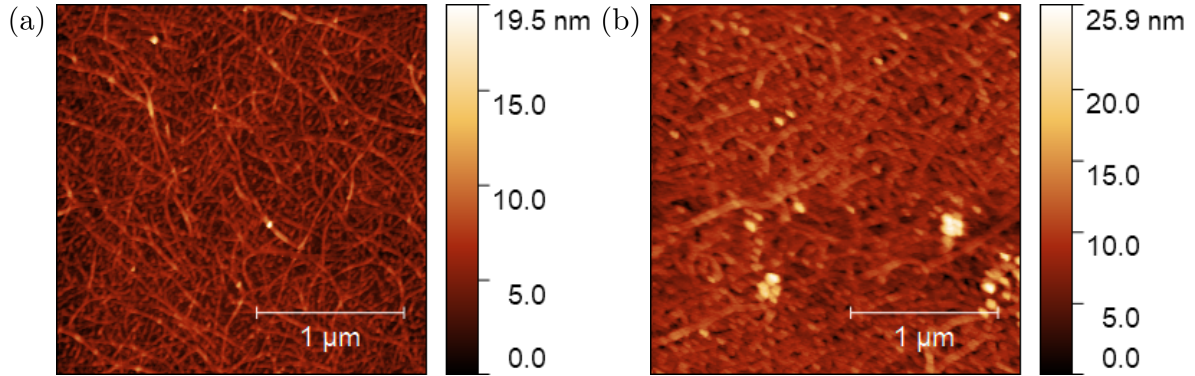


Figure 2: Atomic force microscope images of the channel region of carbon nanotube network devices before and after functionalisation. The channel network of a pristine device is shown in (a), while (b) is of channel 7 from the sensing device functionalised in this section.

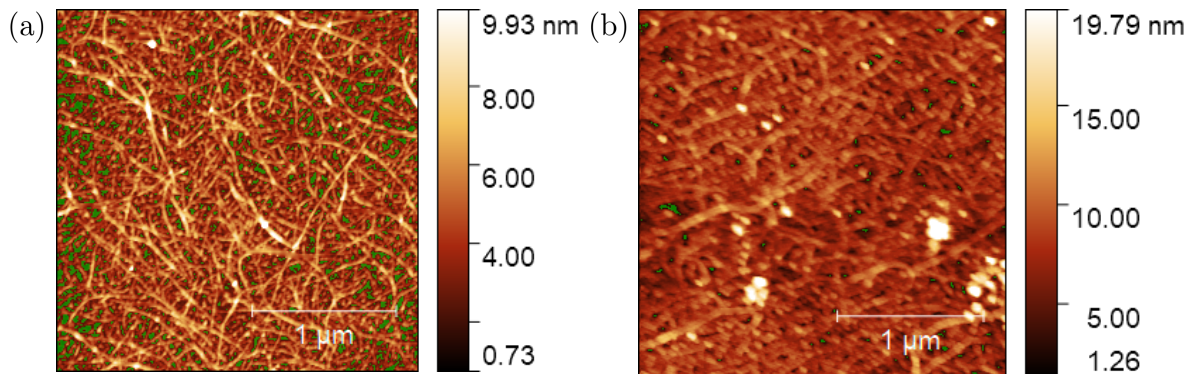


Figure 3: Atomic force microscope images with the substrate background highlighted with a green mask. Here, (a) shows a device channel after functionalisation with PBASE and methanol, while (b) shows channel 7 from the sensing device functionalised with OR22a nanodiscs in this section.

image processing. This height is shown against each carbon nanotube network the masking tool in Gwyddion in Figure 3. In Gwyddion, both images were then simplified to a binary representation, where features above a certain threshold were shown as white and features below shown as black. This representation, shown in Figure 4, has the appearance of a cross-section through the network at the threshold height. The threshold was chosen as the minimum height where carbon nanotube spindles were no longer apparent in the functionalised image, 10 nm above the substrate. Figure 4 (a) shows only a few, sparsely distributed features, each measuring up to 50 nm across. These features may correspond to large nanotube-nanotube junctions, surfactant residue, or other surface contamination (?@sec-pristine-morphology). In Figure 4 (b), many features are over 50 nm across. They are often found close together, and form a curved line across the network in the bottom left corner (shown in red); this arrangement of nanodisc features is similar to that reported previously for OR22a nanodiscs on sparser, more bundled networks [@Murugathas2019b].

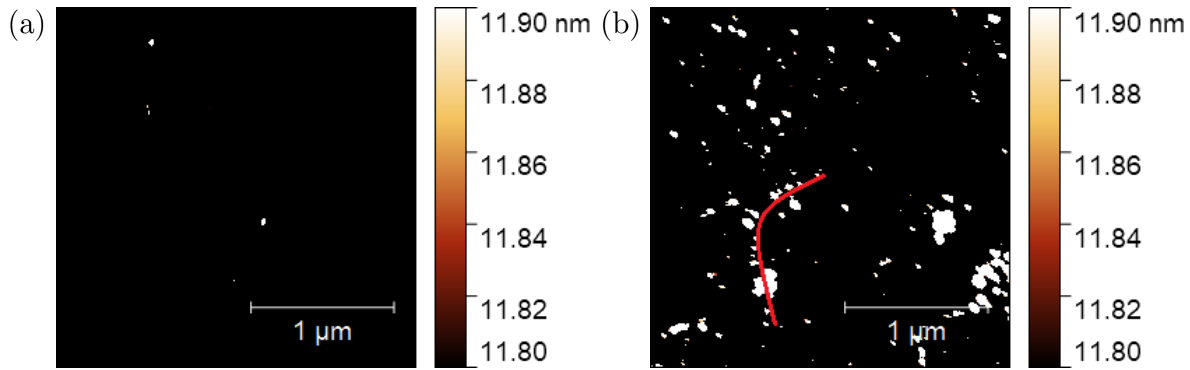


Figure 4: Binary representations of the atomic force microscope images of (a) the pristine device and (b) the functionalised device, with a threshold height of 11.8 nm (10 nm above the average substrate height).

The maximum image height of the OR nanodisc-functionalised channel is 26 nm (Figure 2) and only nanodisc features are present at 12 nm (Figure 4), meaning that nanodisc agglomerates at least 14 nm tall are present on the channel. Assuming a average carbon nanotube height of 1.45 nm, with an average substrate height of 1.8 nm, the nanodisc agglomerates visible in Figure 2 could be up to ~ 23 nm tall. The estimated height range for nanodiscs is $\sim 10 - 20$ nm [@Nath2007; @Bayburt2010; @Murugathas2020]. It is possible that nanodiscs form a single layer on the carbon nanotube network. Height measurements of biological samples taken via AFM have been shown to underestimate actual feature height by over 50% [@Vobornik2023]. Even so, assuming this squishing effect is not significantly in excess of 50%, the agglomerates are only a few nanodiscs high at most. As the nanodisc agglomerates are up to 200 nm across at their widest point (Figure 2), comprising of at least 20 nanodiscs, it appears that the clustering behaviour is primarily across the plane rather than vertical. It appears that, rather than nucleating in solution about a central point prior to attachment, the nanodiscs are individually attaching to preferred locations on the network.

This attachment behaviour can be contrasted with the behaviour observed in the atomic microscope image of agglomerated OR22a nanodiscs taken by Murugathas *et al.* [@Murugathas2019b]. The network is significantly sparser, so the relative extent of clustering at different points is easier to discern. There is clearly significant variation in nanodisc attachment across a single nanotube bundle, and it appears that clustering is more significant at junctions between carbon nanotube bundles. Preferred attachment locations away from junctions could result from the higher reactivity of exposed metallic CNTs [@Cao2009], or from regions which are particularly clean of contamination. Interestingly, while the OR22a nanodisc features seen by Murugathas *et al.* via AFM are similar in breadth to those seen here, OR agglomerates which are at least 53 nm tall are present [@Murugathas2020]. It is unclear why the extent of vertical aggregation differs between this work and that of Murugathas *et al.*, but may be linked to the difference in morphology between the networks used. One possibility is that nanodiscs will preferentially attach to metallic carbon nanotubes, but prefer to attach to each other instead of semiconducting nanotubes. A semiconducting tubes in a highly bundled network may block proteins from accessing metallic tubes in the same bundle, leading to a greater degree of self-attachment.

Fluorescence microscopy was also used to confirm the presence of GFP-tagged odorant receptors on the carbon nanotube network. A device was functionalised using nanodiscs with odorant receptors attached to *Aequorea Victoria* green fluorescent protein (GFP) using the process described at the beginning of this section. When these nanodiscs were used, the functionalisation was performed in darkness, with the odorant receptor nanodisc vial transported under an opaque cover to protect it from light (batch number ND-GFP-OR43b-0002, prepared 12 months earlier). After functionalisation, devices were briefly rinsed with DI water and nitrogen dried to remove dried-down salt residue left by the 1× PBS. A control device was also prepared without the use of PBASE, skipping steps 3 and 4 in the functionalisation process. Fluorescence images of the GFP-OR functionalised and control devices are shown in Figure 5. Note that fluorescence microscope images were taken immediately after functionalisation; devices were transported to the fluorescence microscope room in a foil-wrapped container, and the fluorescence microscope room was kept dark while images were taken.

The silicon dioxide regions in each image appear bright under the GFP filter, indicating attachment between the GFP-OR nanodiscs and the silicon dioxide substrate has occurred. As this device has been annealed, UV exposed and developed before functionalisation, the likelihood this unwanted attachment is to residual photoresist is reduced significantly (see ?@sec-photoresist-contamination). The SiO₂ substrate also appears brighter in the images on the right of Figure 5, which are of the device initially exposed to PBASE. The discussion in ?@sec-pyrene-interactions indicates that the pyrene moiety of PBASE interacts with the silicon dioxide substrate. Assuming no significant variation in the fluorescence of GFP between nanodisc vials, the PBASE coating appears have led to more nanodiscs attaching to the silicon dioxide, giving rise to the brighter fluorescence of the silicon dioxide seen for the PBASE-incubated device on the right of Figure 5.

A comparison of fluorescence in the channel region between images on the left of Figure 5

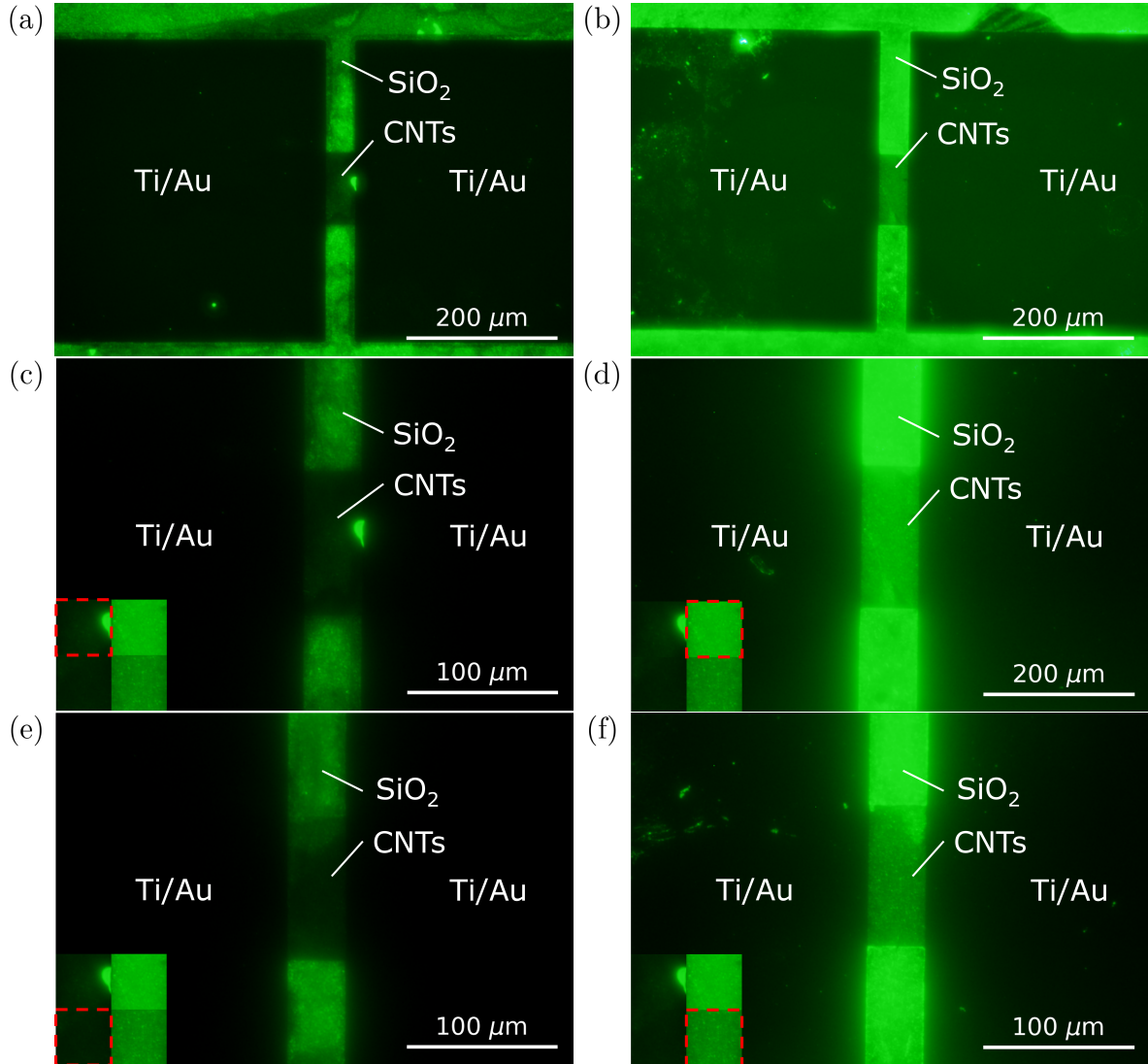


Figure 5: The fluorescence images on the left side – (a), (c) and (e) – show unencapsulated carbon nanotube network channels from a device incubated in GFP-OR nanodiscs. The rectangular dark regions to the left and right of each image are the gold electrodes. The fluorescence images on the right – (b), (d) and (f) – show the channels of a similar device after successive PBASE and GFP-OR nanodisc incubation. Images (a) and (c) are both of the same channel on the first device, and images (b) and (d) are of the same channel on the second, but (c) and (d) were taken using a greater magnification. The insets in (c)-(f) compare the central channel region of (c)-(f) more directly. All images were taken with the same microscope settings (GFP filter and 10 s exposure time), taken in quick succession, directly after functionalisation in a dark room.

(GFP-OR nanodiscs) and the images on the right (GFP-OR nanodiscs and PBASE) is given by the inset in Figure 5 (c)-(f). The inset demonstrates that the channels not incubated in PBASE are significantly less bright than those that had been incubated with PBASE. It appears that the presence of GFP-OR nanodiscs in 1× PBS is limited on these channels. However, when the carbon nanotubes are modified with PBASE, the GFP-OR nanodiscs are able to attach to the channel, and so the channel shows up brightly under the fluorescence microscope GFP filter. Importantly, since the GFP is attached to odorant receptors rather than the nanodiscs themselves, there must be odorant receptors present on the channel after functionalisation; attachment to the channel is not limited to empty nanodiscs. This trend was consistent across all conducting channels on each of the two devices. As far as I know, this is the first time fluorescence has been used to investigate the attachment of odorant receptor nanodiscs to a carbon nanotube network.

Aqueous Sensing of Ethyl Hexanoate

```
dilution_preparation %>%
  kable(
    booktabs = TRUE, #LaTeX "booktabs formatting"
    row.names = FALSE, #remove row labels
    linesep = "" #no linespaces
  ) %>% column_spec(1, width = "2.5cm") %>% column_spec(2, width = "2.5cm") %>% column_spec(3, width = "2.5cm")
```

Table 1: Preparation of analyte dilutions in 1XPBS from solutions of analyte in DMSO. The 1XPBS used was prepared on the same day as the dilution process.

Conc. in DMSO	1XPBS added	Final volume	Final conc.
5 μ L × 0 fM	995 μ L	1 mL	0 fM, 0.5% v/v DMSO
5 μ L × 200 fM	995 μ L	1 mL	1 fM, 0.5% v/v DMSO
5 μ L × 200 pM	995 μ L	1 mL	1 pM, 0.5% v/v DMSO
5 μ L × 200 nM	995 μ L	1 mL	1 nM, 0.5% v/v DMSO
5 μ L × 200 μ M	995 μ L	1 mL	1 μ M, 0.5% v/v DMSO

The procedure used for biosensor detection of ethyl hexanoate in liquid was the same as the procedure outlined in ?@sec-dummy-sensing, except 0.5% v/v DMSO was present in the

buffer solution (to improve ethyl hexanoate solubility) and dilutions of ethyl hexanoate in the same 0.5% v/v DMSO 1× PBS buffer solution were added during the sensing series. The 0.5% v/v DMSO 1× PBS was prepared by adding 5 μ L of DMSO to 995 μ L 1× PBS before device characterisation. The dilutions of ethyl hexanoate were prepared with the same 1× PBS at the same time, where 5 μ L of 200 fM, 200 pM, 200 nM and 200 μ M ethyl hexanoate in DMSO were placed into four individual vials containing 995 μ L 1× PBS each, giving 1mL vials of 1 fM, 1 pM, 1 nM and 1 μ M ethyl hexanoate in 0.5% v/v DMSO 1× PBS. The ethyl hexanoate in DMSO dilutions were prepared beforehand as a 1:10 dilution series in DMSO using 200 mM stock solution, where dilutions ranged from 20 mM to 200 fM. Sampling measurements were taken using the B1500A semiconductor device analyser, with the transfer measurement in Figure 1 (b) taken directly before sensing. The full control series plus sensing sequence is shown in Figure 6. Gate current remained negligible across the entire sensing procedure.

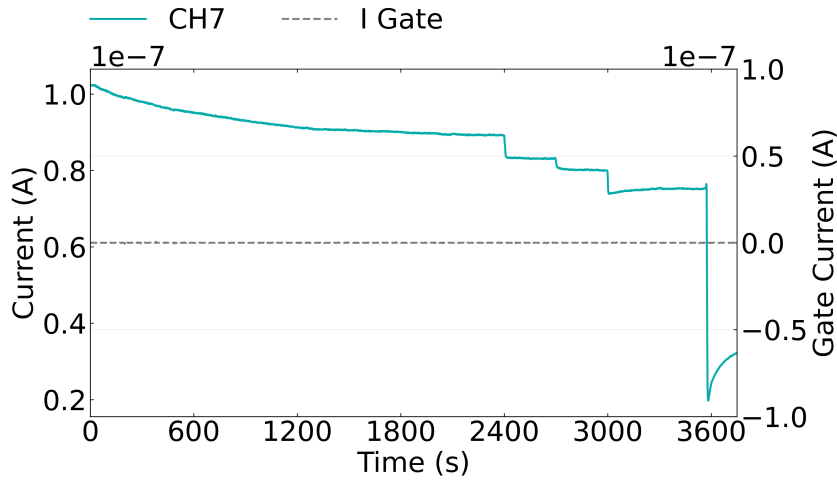


Figure 6: The control series and ethyl hexanoate sensing series of the OR22a-functionalised device channel. Source-drain current was set at $V_{ds} = 100$ mV while gate current was set at $V_g = 0$ V. Functionalisation and sensing was performed using the methods developed in this thesis by Danica Fontein, School of Chemical and Physical Sciences, Te Herenga Waka - Victoria University of Wellington.

The control series for the sensing series is shown in Figure 7 (a). No clear stepwise response is seen to buffer additions or subtractions. The functionalised device shows similar baseline drift behaviour to that of a pristine device, with a period of short-term decay quickly yielding to a more long-lived decay behaviour. A linear fit $I = c_1 t + c_2$ to the region 1200 – 1800 s had a gradient of $c_1 = -1.76 \pm 0.02$ pA/s. This gradient is smaller than the range of values found for the linear fit approximating the longer-term drift of a pristine device ([?@sec-baseline-drift](#)), but of the same order of magnitude. The linear fit was then subtracted from the control series and an exponential fit $I = I_0 \exp(-t/\tau)$ was performed on the remaining dataset, as shown in Figure 7 (b). A value of 590 ± 3 s was found for the exponential time constant, similar to those found for the channels of the pristine device. This confirms that the 1800 s control series

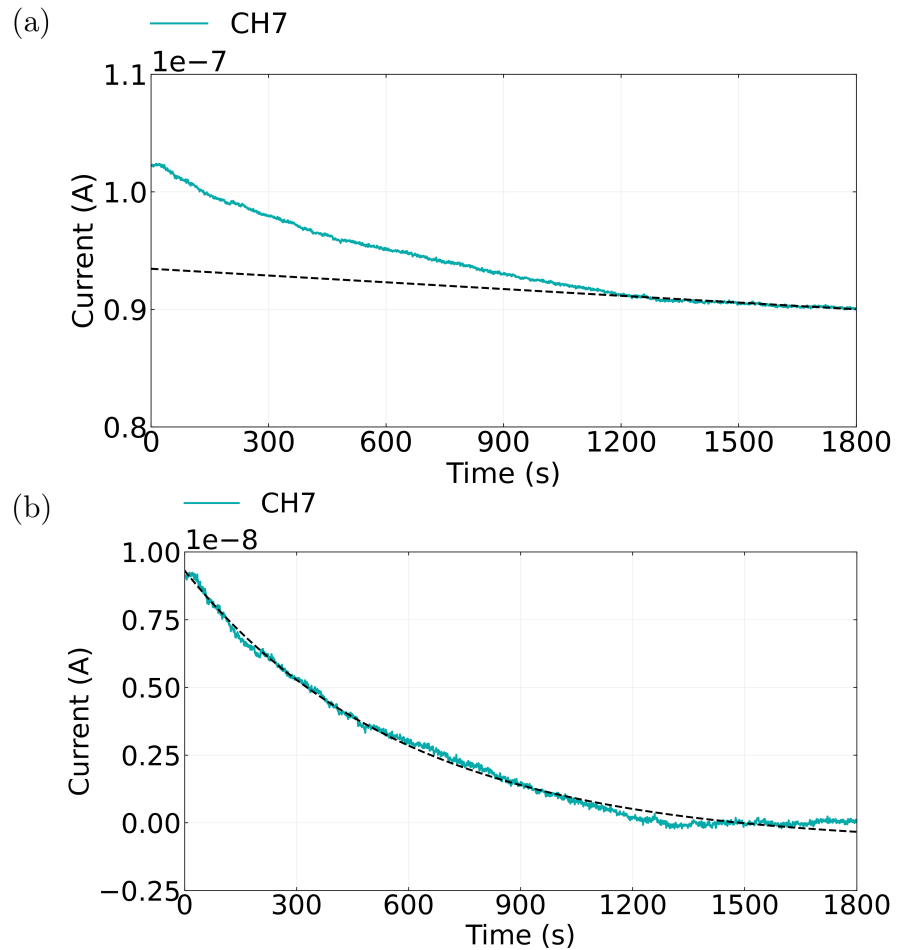


Figure 7: The control series for the OR22a-functionalised device is shown in (a), alongside an extrapolated linear fit to the control series from 1200 s onwards. The control series with the linear approximation subtracted fitted to an exponential curve is shown in (b).

is sufficient to avoid the presence of short-term decay during sensing.

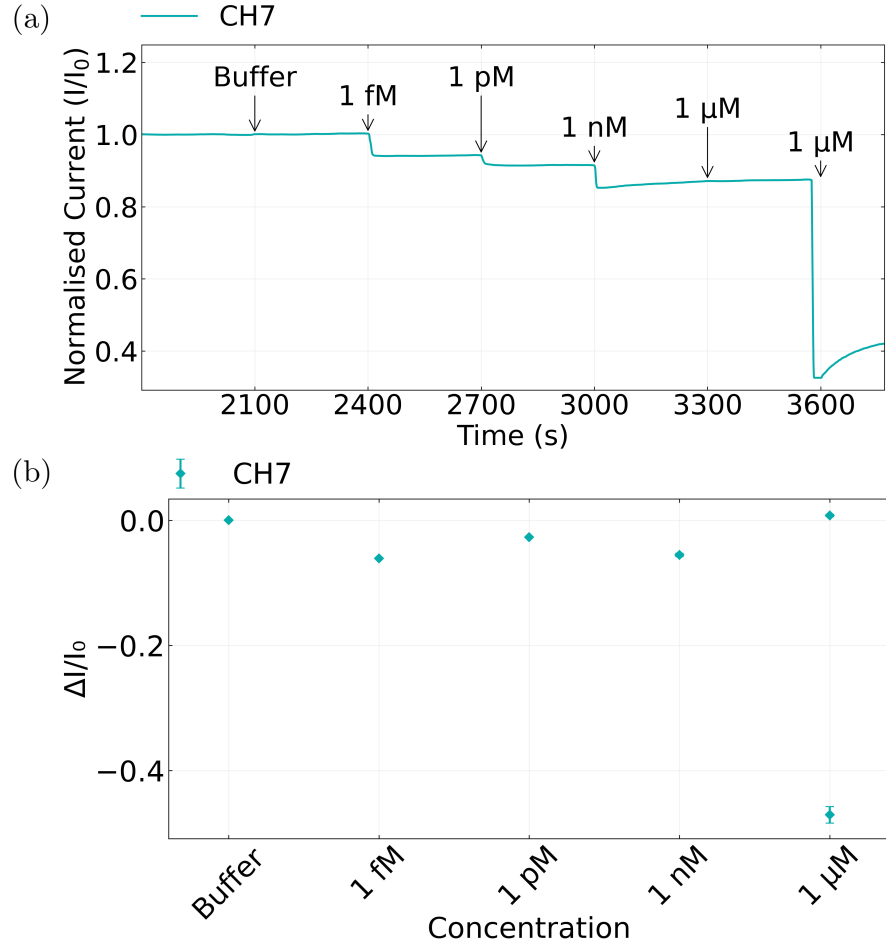


Figure 8: The normalised sensing series for the OR22a-functionalised device is shown in (a). The current data has been despiked, with baseline drift removed and a moving median filter applied. The concentration of each $20 \mu\text{L}$ addition is indicated above the time of addition. The signal data corresponding to the mean difference in current before and after each addition is shown in (b).

It appears that the exponential fit overestimates current measurements between 1100 s and 1500 s and underestimates measurements between 1500 s and 1800 s. This deviation from the fit may result from the linear approximation used to represent long-term baseline drift being weaker for this channel than for those discussed previously in [?@sec-dummy-sensing](#) and [?@sec-pristine-EtHex](#). This could result from the exponential terms for long-term baseline drift having relatively short time constants, so $t \ll \tau_i$ no longer holds and higher order terms in the linear approximation are no longer negligible. This observation may indicate a relationship exists between device functionalisation and the long-lived device decay behaviour. However,

it may simply result from the natural variation between randomly-deposited device channels. Further work may be required to confirm the existence of such a relationship, though this work is outside the scope of this thesis.

Figure 8 (a) shows the cleaned and filtered ethyl hexanoate sensing data from the OR22a-functionalised device from 1800 s onwards. The concentration of each 20 μ L addition is indicated above the corresponding addition time. The source-drain current across the channel decreased rapidly with each addition of ethyl hexanoate in 0.5% v/v DMSO 1 \times PBS solution. This current decrease appears irreversible, as the current stabilises after each addition at a lower current level than prior to the addition. This behaviour appears to be a response by OR22a to its positive ligand ethyl hexanoate, similar to the response by OR22a to methyl hexanoate seen by Murugathas *et al.*. The ORCO coreceptor was not required to be present for responses to be seen. The device showed responses to ethyl hexanoate over a wide range of concentrations, beginning with a \sim 6% response to 1 fM EtHex in 0.5% v/v DMSO 1 \times PBS, with a maximum response of \sim 45%. Interestingly, as seen in Figure 8 (b), no clear dose-dependent response was observed. The behaviour seen may be explained by a decreased sensitivity to subsequent additions seen by Murugathas *et al.* [Murugathas2019b] competing with the logarithmic increases in the concentration around the channel.

Addressing Biosensor Variability

Variability in Biosensor Behaviour

Despite the successful detection of ethyl hexanoate by an OR22a nanodisc-functionalised biosensor in Section , it was found that this behaviour was not readily reproducible. The results from the previous section were not repeated when using the same procedure for fabrication of devices alongside an identical functionalisation process with the same batch of OR22a nanodiscs (ND-OR22a-SB018). The ethyl hexanoate sensing sequence from six functionalised device channels is shown in Figure 9. Figure 9 (a) has been left unfiltered to illustrate the variation in behaviour between channels, while Figure 9 (b) has been prepared in the same manner as Figure 8 (a). The current response to each analyte addition is similar to that seen after the initial addition without ethyl hexanoate present. The largest contributing factor to current change appears to be drift. Unlike the clear decreases in current subsequent to ethyl hexanoate additions seen in Figure 8 (a), no decreases are seen in Figure 9 (b) to any ethyl hexanoate solution addition.

Liquid-gated electrical characteristics were taken of each sensing channel from this device before and after functionalisation with OR22a nanodiscs, in the same manner as Section . These characteristics are shown in Figure 10. The average threshold shift was -0.06 ± 0.02 , the same as that of a device functionalised with PBASE in methanol without subsequent functionalisation with OR22a nanodiscs. To test whether protein was present on the channel, an atomic force microscope image was taken of channel 6, as shown in Figure 11. The same image analysis as in Section was performed, with the substrate mask shown in Figure 12 (a)

giving an average substrate height of 3.8 ± 0.4 . A binary representation of the image with a 12.5 nm threshold, 8.7 nm above the average substrate height, is shown in Figure 12 (b). As with the functionalised device in Figure 4 (b), Figure 12 (b) shows clustering of features, many of which are larger than 50 nm across. It seems, therefore, that nanodisc aggregates up to 27.5 nm high are present on channel 6, despite the lack of a significant threshold shift as a result of functionalisation.

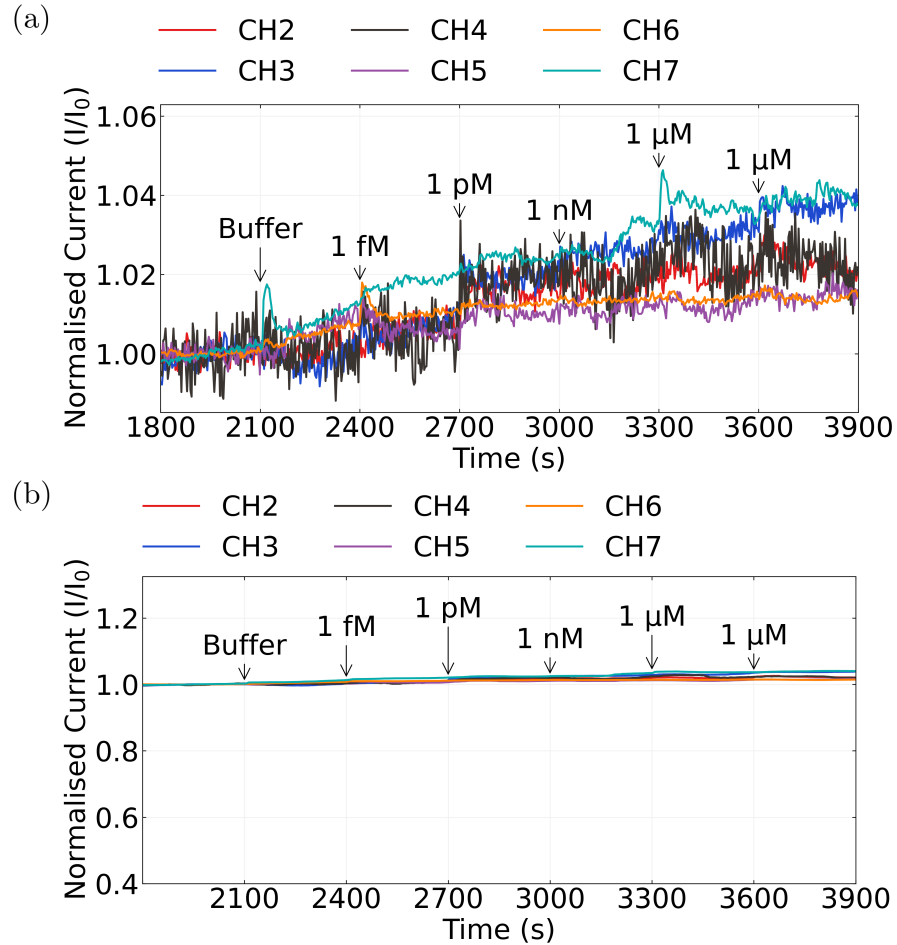


Figure 9: The normalised sensing series of another OR22a-functionalised device across six multiplexed channels, where current data has been despiked and baseline drift removed. The concentration of each 20 μL addition is indicated above the time of addition. The same sensing series is shown in both (a) and (b), where a moving median filter has been applied in (b).

Both OR nanodisc and empty nanodisc attachment via PBASE have been shown to cause significant gating of the network (Section). Therefore, it might be reasoned that the lack of a gating effect, but with nanodiscs present, results from a direct attachment mechanism

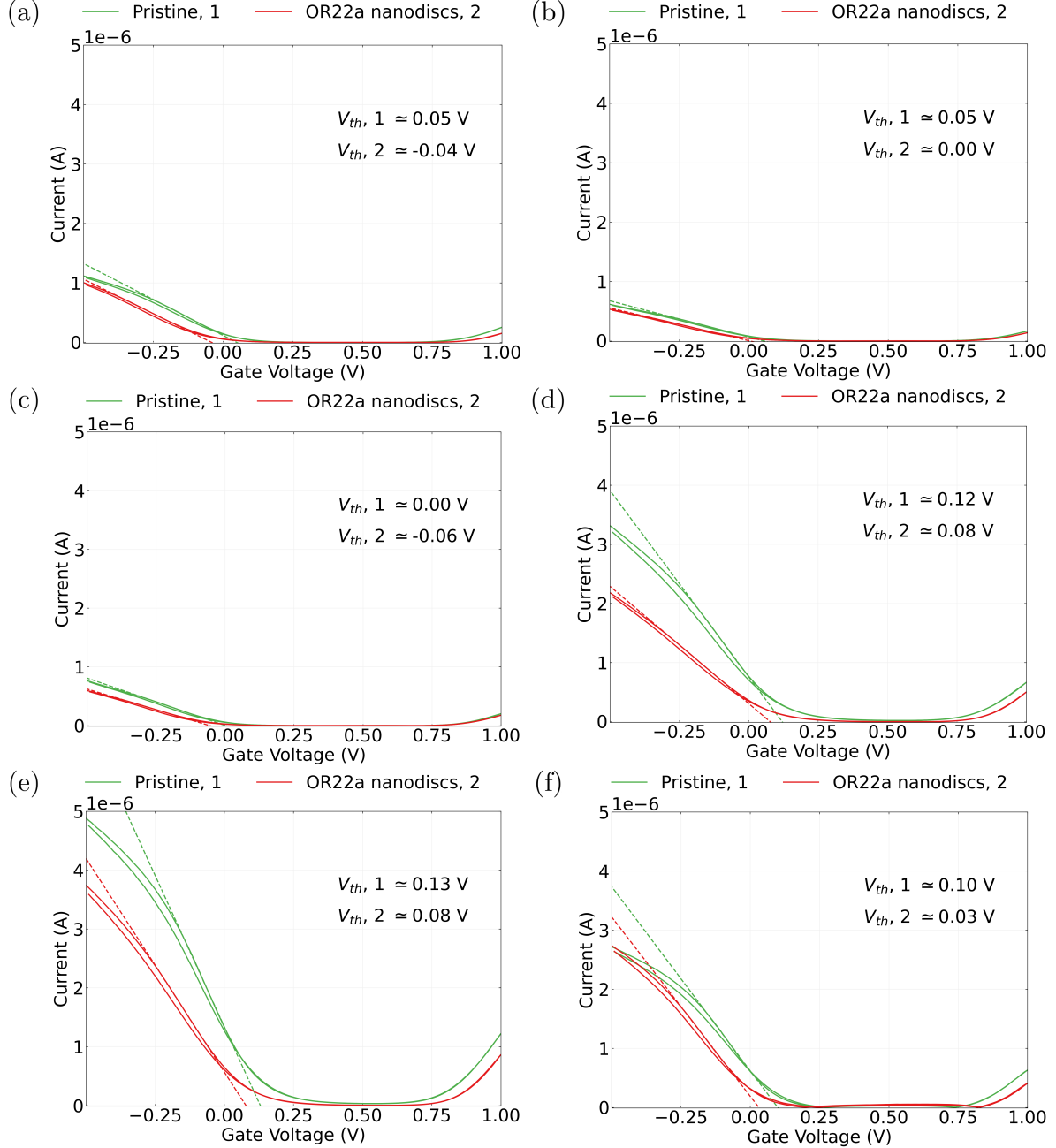


Figure 10: Liquid-gated carbon nanotube network device transfer characteristics before and after OR22a nanodisc functionalisation. Source-drain current was $V_{ds} = 100$ mV for both the forward and reverse sweep. Each subfigure (a)-(f) corresponds to a different channel of the functionalised device; (a) corresponds to channel 2, (b) corresponds to channel 3, (c) corresponds to channel 4, (d) corresponds to channel 5, (e) corresponds to channel 6 and (f) corresponds to channel 7. The dashed line shown is tangent to the subthreshold slope of the characteristic curve. The threshold voltage corresponding to the intercept of this slope with the x-axis is shown for each transfer characteristic curve.

circumventing the PBASE linker. The amine group on proteins can be attached directly onto carbon nanotubes by adsorption, although this attachment is relatively weak [Bradley2004]. Figure 13 shows an AFM image of a carbon nanotube network film after submersion in a 10 $\mu\text{L}/\text{mL}$ OR22a nanodisc in PBS solution for 1 hour (batch NDOR22a-0016-1), without prior exposure to PBASE in methanol. Figure 14 shows the substrate mask in (a) and a binary representation of this AFM with nanodisc aggregates clearly visible in (b). In Figure 15 (a), the negative threshold shift of a channel modified in this way was -0.27 V, similar in size to the shift due to functionalisation seen for the working biosensor.

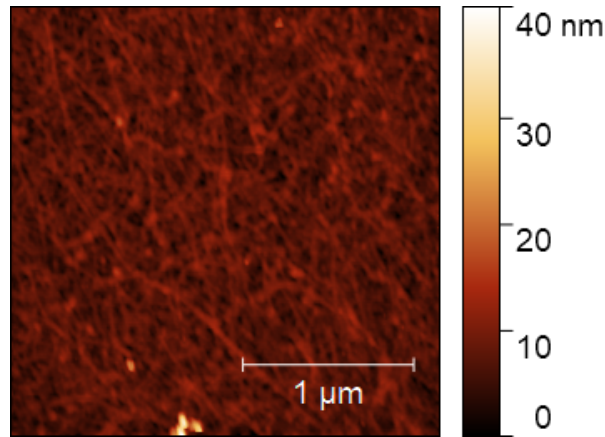


Figure 11: An atomic force microscope image of channel 6 from the OR22a nanodisc functionalised device which showed no response to ethyl hexanoate.

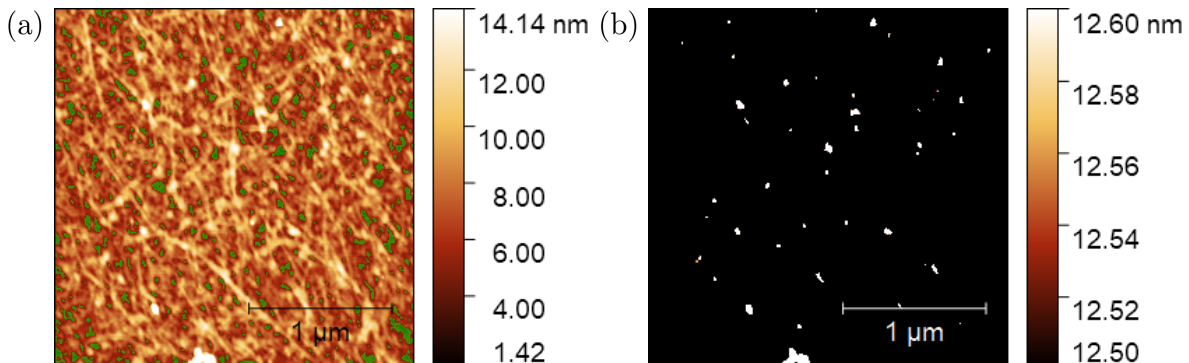


Figure 12: The mask used to find the average substrate height of the functionalised channel 6 is shown in (a), with the substrate highlighted green. The bounds of the colour map have been lowered in (a), as colour mapping over the full height range makes it difficult to clearly distinguish between sub-20 nm features and the substrate. A binary representation of the atomic force microscope image with a threshold height of 12.5 nm is shown in (b).

The attachment of nanodiscs in 1 \times PBS may seem surprising, given that the fluorescence

microscopy work in Section indicates no GFP-OR present after functionalisation without PBASE. However, this device channel did not work as a sensor when tested with ethyl hexanoate. Figure 15 (b) shows a small, positive current response to additions of ethyl hexanoate diluted in 1% v/v DMSO 1× PBS, which may result from the weakly attached OR22a nanodiscs being mechanically removed by the pressure of each addition on the device channels.

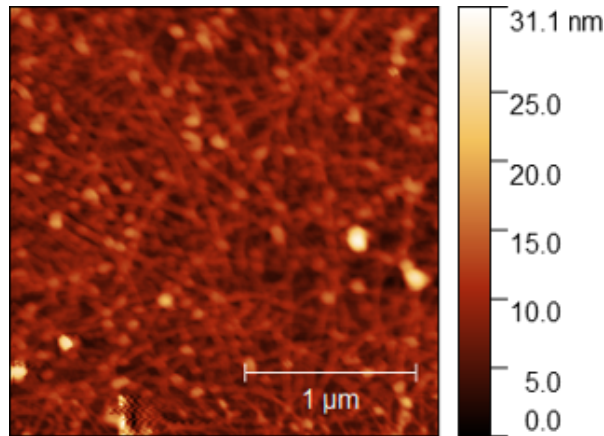


Figure 13: An atomic force microscope image of a carbon nanotube film submerged in OR22a nanodiscs for 1 hour without prior exposure to PBASE or methanol.

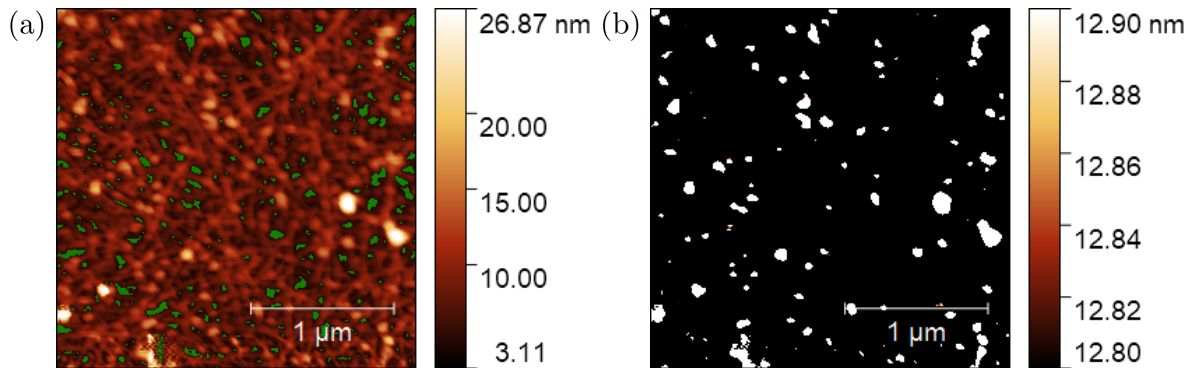


Figure 14: The binary representation of the network, with a height threshold of 12.8 nm (average substrate height = 4.1 nm), is shown in (b).

An explanation is required for the seemingly contradictory situation where nanodiscs can be present on a device channel without significant gating effects. The most straightforward explanation is that no reliable correlation exist between the two phenomena. Given the consistent threshold shift results for various linker functionalisations seen in ?@sec-noncovalent-functionalisation, this scenario implies a significant variation in protein structure and charge behaviour within a single nanodisc batch, which seems unlikely. Another possibility is that some type of surface coating is causing nanodiscs to not attach to either PBASE or the carbon nanotubes. This surface coating might be attractive, attaching to both nanodiscs and

carbon nanotubes, but forming a barrier layer between the two. Alternatively, this coating might be repulsive, causing nanodiscs to attach weakly to the substrate around the carbon nanotubes. Variations in the degree to which a network is coated may then explain why the same functionalisation method might work for one device but not another. The following section investigates ways of eliminating possible sources of surface coating for more reliable functionalisation results.

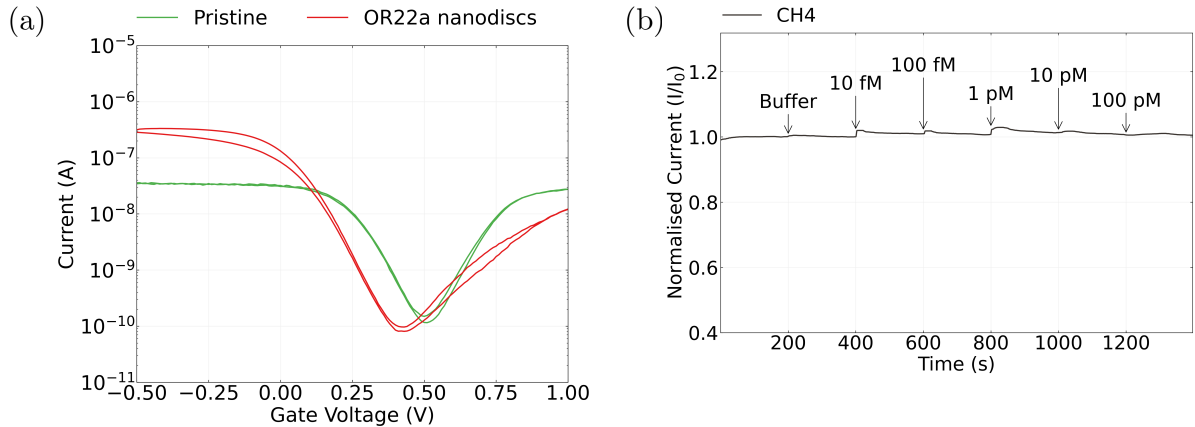


Figure 15: The device characteristics in (a) are from channel 4 of the device placed in OR22a nanodisc solution for 1 hour without prior exposure to PBASE or methanol before and after functionalisation. Real-time sampling using this channel is shown in (b). A 20 μ L addition of 1% v/v DMSO 1 \times PBS was made at 200 s. Subsequently, 20 μ L additions of ethyl hexanoate diluted in 1% v/v DMSO 1 \times PBS were made at 400 s, 600 s, 800 s and 1000 s and 1200 s, with the concentration of each addition indicated above the time of addition.

Potential Sources of Variability

Throughout the course of this thesis, multiple potential candidates for the unwanted surface coating discussed in the previous section have been identified. These include the surfactant used in carbon nanotube deposition ([?@sec-pristine-morphology](#), [?@sec-pristine-electrical-characterisation](#)), the solvent used in functionalisation ([?@sec-PBASE-electrical-characterisation](#)), residual photoresist ([?@sec-photoresist-contamination](#)), and the hydrophobic layer which naturally forms on graphene and carbon nanotubes in air ([?@sec-hydrophobicity](#)). Another possibility is that PBASE itself is acting as a surface coating, which could result from multilayer coverage restricting access by the odorant receptors to directly attached PBASE ([?@sec-PBASE-attachment](#)). Alternatively, PBASE may have hydrolysed into PBA prior to attachment, forming an inert surface layer upon π -stacking around the carbon nanotubes. However, no threshold shift directly attributable to PBA attachment should occur ([?@sec-PBA-characterisation](#)), and this is not what

was observed when characterising the non-working device in Section . To understand which of these candidates is responsible for the significant variability in biosensor functionality, the sensing procedure was performed with slight variations on the biosensor fabrication and functionalisation procedures. In each test, an individual element of one of these procedures was altered to prevent the introduction of a specific surface coating. The biosensor was then characterised and tested to see if it would respond to its target odorant.

* Spurious Responses

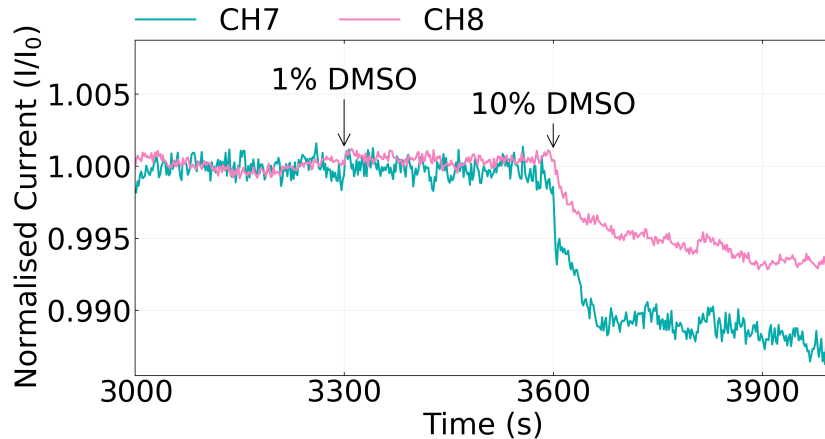


Figure 16: Response to changing the concentration of DMSO in the PDMS well of a OR22a-functionalised sensor. Source-drain current was set at $V_{ds} = 100$ mV while gate current was set at $V_g = 0$ V. The well originally contained 100 μL of 1% v/v DMSO 1X PBS. 20 μL additions of DMSO in PBS were made at 3300 s and 3600 s.

Before testing to see if a surface coating was responsible for the lack of response seen to ethyl hexanoate by the device in Section , it was important to investigate the possibility the signals seen in Section were false positives. The highly sensitive device channel could credibly respond to three different rapid environmental changes occurring with each addition: the mechanical action of the addition, a difference between the 0.5% v/v DMSO in 1× PBS containing the analyte and the 0.5% v/v DMSO in 1× PBS already in the well, or a direct response to analyte. It is important to eliminate the first two possibilities to be certain that the device is responding to analyte. The control series as it stands demonstrates responses cannot be explained by mechanical action. All analyte solutions are prepared simultaneously using the same 1× PBS, taking care to avoid cross-contamination, so responses are unlikely to result from a difference between the 1× PBS in the analyte solution and the 1× PBS in the well. It then must be verified whether a functionalised device channel will respond to a change in DMSO concentration, which is the result of the DMSO concentration in an analyte addition being different to the concentration in the PDMS well.

Figure 16 shows that a increase in DMSO concentration in the well from 1% v/v to 2.5%

v/v leads to a steep drop in current of 0.5% – 1.5% across two OR22a-functionalised device channels. The gate current remained negligible across this time period (<0.1% of average drain current).

Though the current changes in Figure 16 share similarities with other observed responses to analyte, they are significantly smaller than the >2% changes seen in Section . Furthermore, precise measurement of DMSO in analyte preparations means that a change in proportion of DMSO in the well of this scale is unlikely. It therefore seems improbable that a change in DMSO concentration is the primary cause of these responses. However, the author recommends a slight modification to the control series for a more robust experimental baseline. For a device with 100 μ L 0.5% v/v DMSO 1× PBS in the well after the first buffer addition at 100 s, a subsequent 20 μ L addition of 1% v/v DMSO 1× PBS at 200 s and 20 μ L addition of 0% v/v DMSO 1× PBS addition at 300 s can be used to check for spurious responses due to changing DMSO concentration, while ensuring the DMSO concentration in the well is 0.5% v/v after the control series.

* Fabrication

Two different approaches were trialled to eliminate possible surfactant contamination, both of which drew heavily on previous methods used for iOR biosensor fabrication [@Murugathas2019b; @Murugathas2020]. Solvent-deposited carbon nanotube network and graphene devices were fabricated as described in ?@sec-qw-processing. The same functionalisation process for each device was used as described in Section with OR22a nanodiscs.

The normalised sensing behaviour for the solvent-deposited carbon nanotube device is shown in Figure 17. The device shows a small current increase on four channels with the 10 fM ethyl hexanoate addition, and a small decrease on five channels with the 100 fM EtHex addition. No current change exceeded 2%, and as shown in Figure 17 (b), the current changes appear negligible on the scale of the changes seen in Section . The average threshold shift from functionalisation was -0.02 ± 0.01 V, which indicates attachment of PBASE but not nanodiscs. As the device was made using the pre-2023 encapsulation mask, an AFM was taken of a separate film modified in the same manner, shown in Figure 19 (a). The average substrate height was 11.3 ± 0.9 nm. A binary representation of the image taken at the minimum height no spindle-like bundles were visible, 46.1 nm, is shown in Figure 19 (b). Attached nanodisc aggregations are clearly visible, and appear closer in nature to those observed for an OR35a-functionalised film [@Murugathas2020] than previously seen in this work. Figure 19 (c) and (d) show that over a larger scale these aggregations can be at least 330 nm tall, forming large clusters which may indicate mutual interaction during deposition.

The electrical characteristics of a graphene device channel before and after functionalisation with OR22a nanodiscs in the manner outlined previously are shown in Figure 20 (a), showing an order of magnitude decrease in on-current and a negatively shifted Dirac point with functionalisation, as seen previously for working OR22a nanodisc GFET biosensors [@Murugathas2020]. Figure 20 (b) shows when the process is repeated on another device without

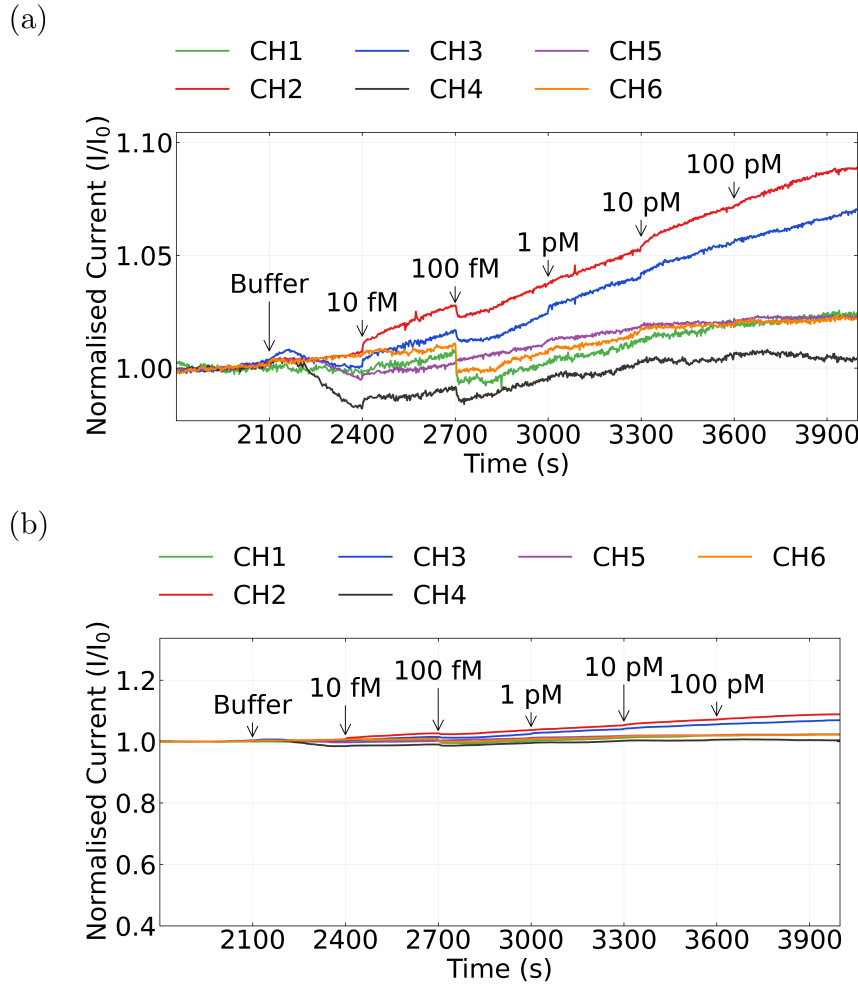


Figure 17: The normalised sensing series of the solvent-deposited, OR22a-functionalised device across six multiplexed channels, where current data has been despiked and baseline drift removed. Source-drain current was set at $V_{ds} = 100$ mV while gate current was set at $V_g = 0$ V. The concentration of each 20 μL addition is indicated above the time of addition. The same sensing series is shown in both (a) and (b), where a moving median filter has been applied in (b).

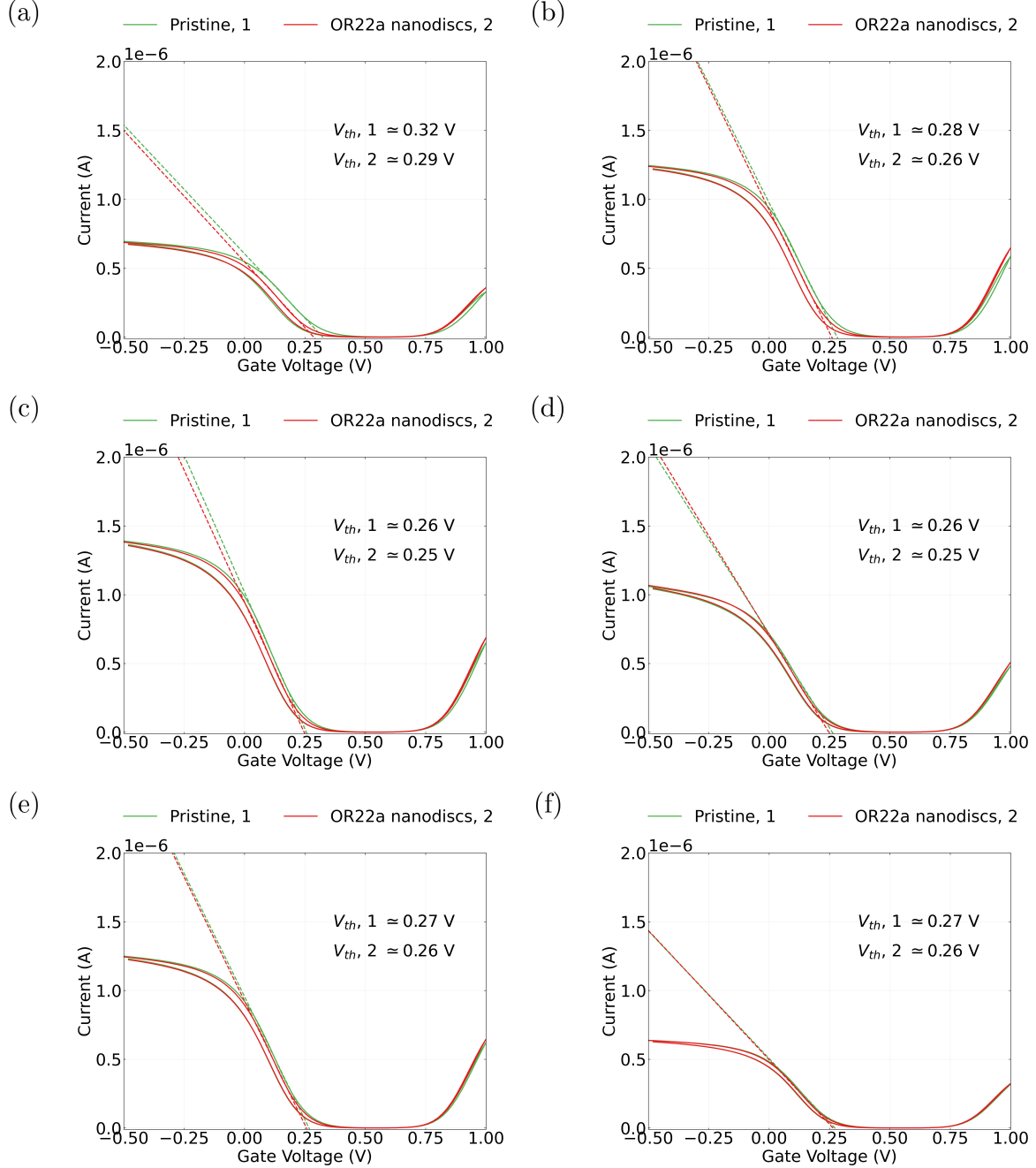


Figure 18: Liquid-gated solvent-deposited carbon nanotube device transfer characteristics before and after OR22a nanodisc functionalisation. Source-drain current was $V_{ds} = 100$ mV for both the forward and reverse sweep. (a) corresponds to channel 2, (b) corresponds to channel 3, (c) corresponds to channel 4, (d) corresponds to channel 5, (e) corresponds to channel 6 and (f) corresponds to channel 7. The dashed line shown is tangent to the subthreshold slope of the characteristic curve. The threshold voltage corresponding to the intercept of this slope with the x-axis is shown for each transfer characteristic curve.

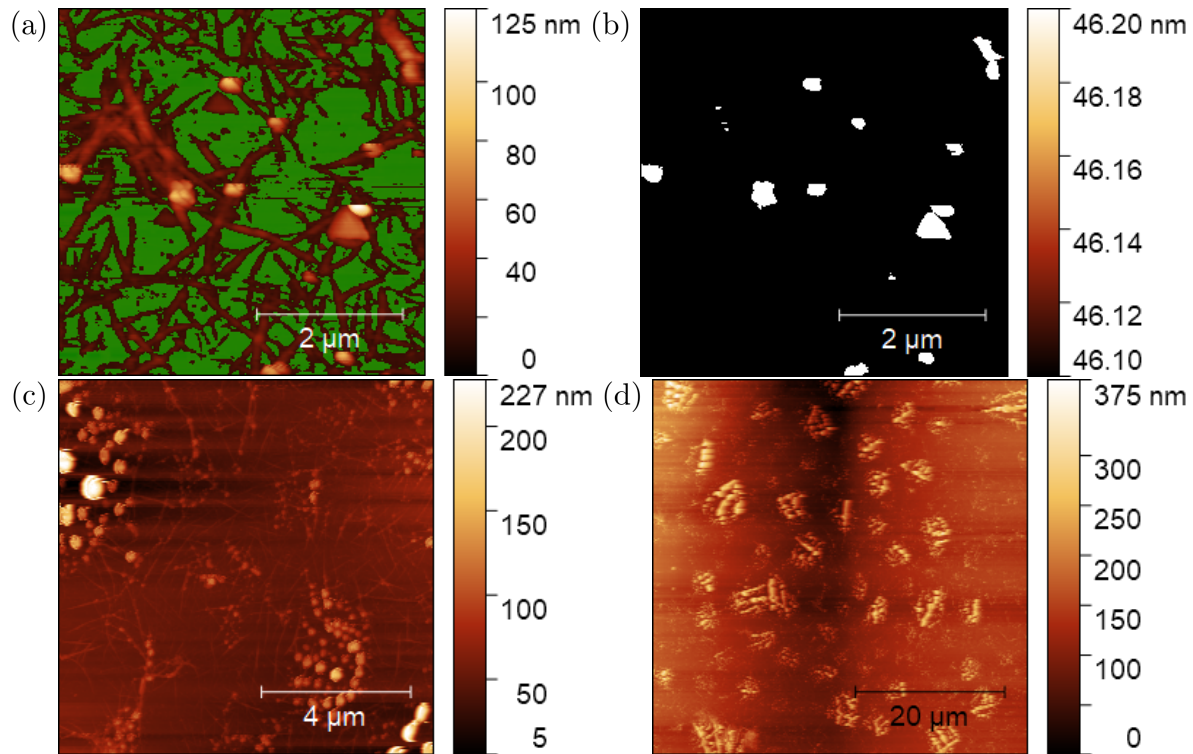


Figure 19: An $2.5 \mu\text{m} \times 2.5 \mu\text{m}$ atomic force microscope image of an OR22a nanodisc functionalised solvent-deposited carbon nanotube film is shown in (a), with the average substrate height highlighted green. A binary representation of the atomic force microscope image with a threshold height of 34.7 nm is shown in (b). $10 \mu\text{m} \times 10 \mu\text{m}$ and $50 \mu\text{m} \times 50 \mu\text{m}$ atomic force microscope images of another film functionalised in the same manner are shown in (c) and (d) respectively.

initial exposure to PBASE and methanol, a larger negative shift in the Dirac point is observed. It appears the initial functionalisation with PBASE and methanol decreases the charge transferred to the graphene when the nanodiscs are introduced; the difference between these two surface modifications is analogous to that seen for the carbon nanotube devices in Section . A pristine graphene surface and a OR22a-functionalised graphene surface are shown in Figure 21 (a) and (b) respectively. Graphene folds of up to 7.3 nm in height are visible on the right hand side of Figure 21 (a). When functionalised with OR22a nanodiscs, the surface is densely coated with nanodisc aggregates up to ~ 250 nm across and ~ 30 nm tall. These nanodiscs are a similar height and size to those observed by Murugathas *et al.* [@Murugathas2020].

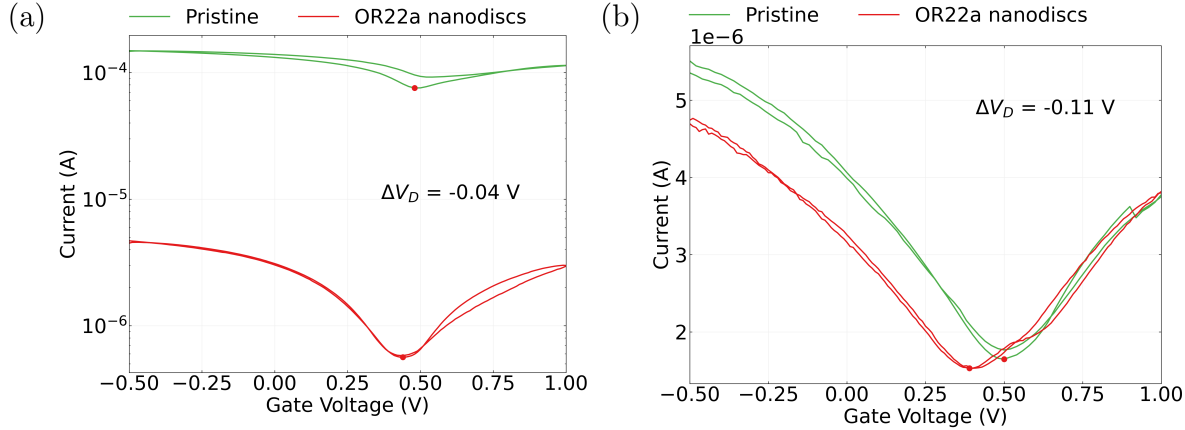


Figure 20: Liquid-gated graphene device transfer characteristics before and after OR22a nanodisc functionalisation, where (a) was functionalised using the standard method while (b) was functionalised without submerging the device in PBASE and methanol. Source-drain current was $V_{ds} = 100$ mV for both forward and reverse sweeps. The shift in Dirac point resulting from functionalisation is also shown for each device.

Both the transfer characteristics and atomic force microscope image indicates widespread attachment of nanodiscs. However, the normalised current data from a OR22a nanodisc graphene field-effect transistor in Figure 22 shows current changes of <1% in response to ethyl hexanoate additions. This contrasts with the OR22a nanodisc-functionalised graphene device behaviour observed by Murugathas *et al.*, where target analyte additions with concentration above 10 fM consistently caused current changes of above 2% [@Murugathas2020]. Again, there appears to be an unresolved functionalisation issue that is not clearly captured either by the atomic force microscope images or the transfer characteristics before and after functionalisation of the graphene devices.

It appears that avoiding the use of surfactant on the transducer element is not sufficient to ensure consistent iOR biosensor functionalisation; it therefore seems likely that a surfactant coating is not the primary reason for the observed variability in device operation. Furthermore,

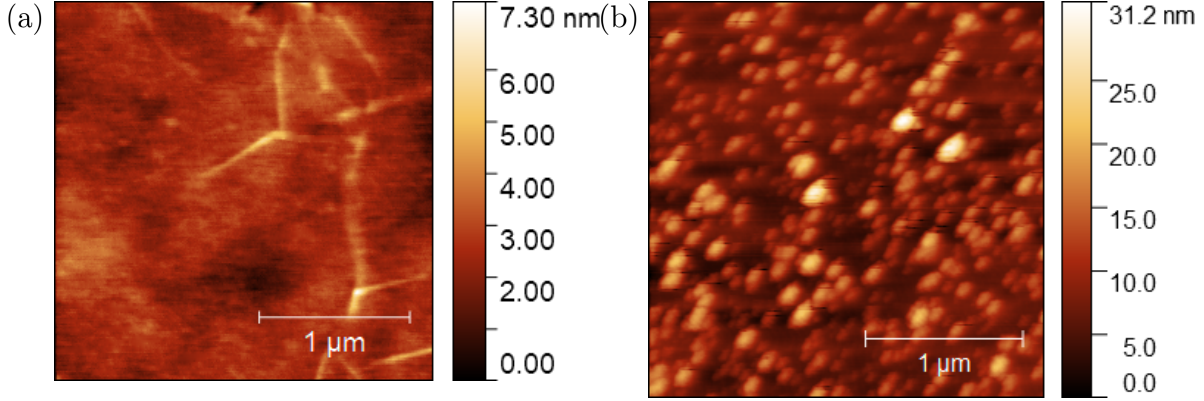


Figure 21: $2.5 \mu\text{m} \times 2.5 \mu\text{m}$ atomic force microscope images of (a) a monolayer graphene film on SiO_2 and (b) a graphene film after OR22a nanodisc functionalisation.

the confounding factor appears to persist across multiple transducer morphologies which show significant variations in both their active surface area and electrical properties.

* Functionalisation

Next, an investigation was made into whether the type of solvent used in functionalisation was responsible for the variability observed in device behaviour. A solvent commonly used in the literature for functionalisation with PBASE is dimethyl sulfoxide (DMSO), as discussed in [?@sec-PBASE-attachment](#). A surfactant-deposited device was functionalised with OR22a nanodiscs in the same manner as described in Section , except DMSO was used instead of methanol when preparing the PBASE solution. The sensing dataset from the four device channels of a suitable current level are displayed in Figure 23 (a), where methyl hexanoate (MeHex) was used as the target compound. No channel shows a negative current response to MeHex. Current changes after each addition are consistently below 1% on all channels, and therefore appear negligible on the scale used in Figure 23 (b).

An atomic force microscope images of a film modified using DMSO in PBASE with OR22a nanodiscs is shown in Figure 24 (a), along with a mask in green indicating an average substrate height of 3.6 ± 0.6 . The binary representation in Figure 24 (b) shows long, rounded features sit directly above the above the CNT threshold height of 12.3 nm. By extending the threshold height range to 12.3 – 18.9 nm, it becomes apparent that these features are not simply large carbon nanotube bundles, but instead appear to be densely packed collections of nanodisc aggregates following the length of various carbon nanotube bundles. The distribution of nanodiscs along the nanotubes gives them a string of pearls or *Hormosira*-like appearance [\[@NewZealandPlantConservationNetwork\]](#). Some features are too tall for the “pearls” on the “string” to be individually distinguished in Figure 24 (c), but Figure 24 (d) shows every rounded “pearl” along every “string” can be distinguished from one another at a taller thresh-

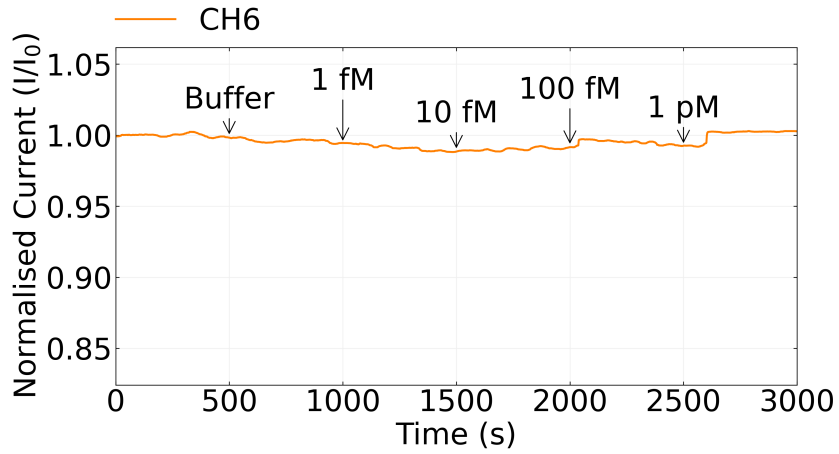


Figure 22: A normalised ethyl hexanoate sensing series taken with a OR22a-functionalised graphene device. Source-drain current was set at $V_{ds} = 100$ mV while gate current was set at $V_g = 0$ V. The concentration of each 20 μL addition is indicated above the time of addition, with additions made at 500 s, 1000 s, 1500 s, 2000 s and 2500 s.

old. These images strongly suggest nanodisc aggregates are present on the network, but does not necessarily indicate a direct connection between nanodiscs and the network.

The transfer characteristics of the four sensing channels are displayed in Figure 25. An average threshold shift of -0.22 ± 0.03 V is seen across these channels, significantly exceeding the expected threshold shifts of -0.06 ± 0.01 for exposure to PBASE in DMSO and -0.15 ± 0.01 for exposure to DMSO without PBASE. This functionalisation threshold shift is similar to that of the device which responded to target analyte in Section , -0.20 V. The shift is also similar to that seen for the device functionalised directly with OR22a nanodiscs without PBASE, -0.27 V. It therefore seems that the nanodiscs are directly attached to the carbon nanotube network, yet they do not respond to the target analyte. It seems likely that the negative gating is a result of nanodisc attachment to the network, either with or without PBASE as a linker; meanwhile, there is limited or no attachment between the network and the odorant receptors themselves. This lack of connection to the odorant receptors appears to be a second factor at play in the variability seen in biosensor behaviour.

As discussed in ?@sec-PBASE-purity, DMSO is a highly hygroscopic solvent. If a non-negligible amount of water is present in the DMSO during functionalisation, the PBASE is being exposed to water for more than an hour before introducing OR nanodiscs. Over this time period, the PBASE may be able to undergo ester hydrolysis [@Hermanson2013-3]. To eliminate the possibility that hydrolysis has prevented the attachment of odorant receptors to PBASE on the network, an alternative method using 1-pyrenebutyric acid (PBA) in DMSO was also trialled. This method was similar to those seen in ?@sec-PBA. PBA is first attached to the carbon nanotube network, then, once the bulk of the DMSO has been rinsed off the device

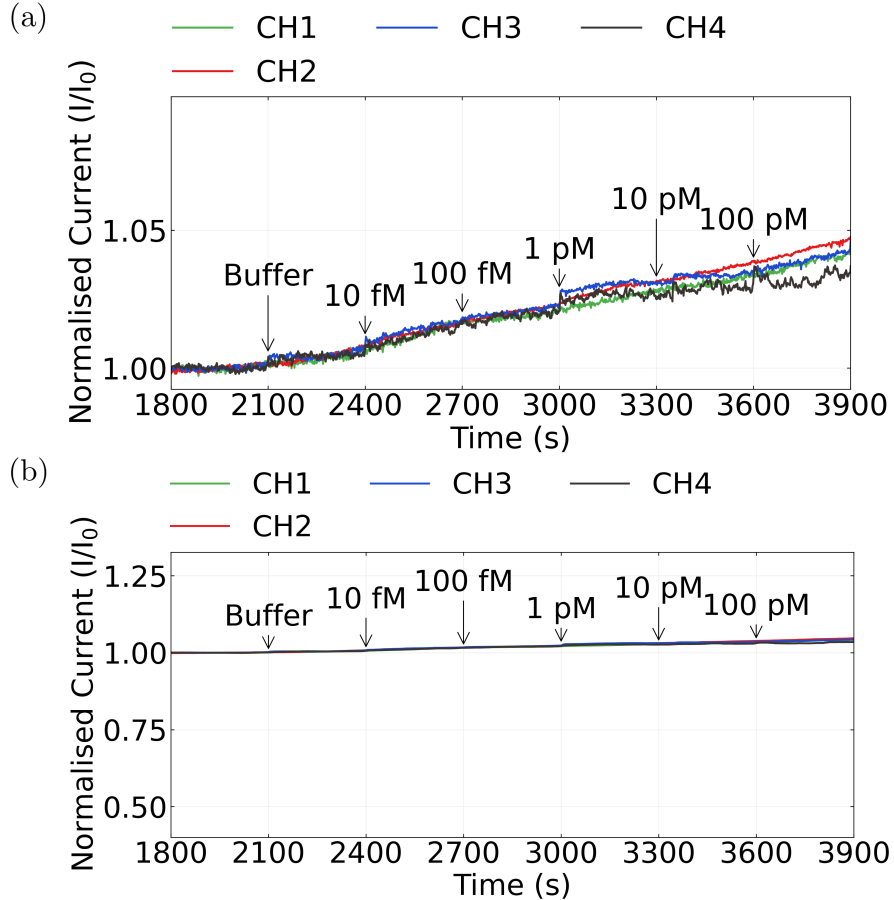


Figure 23: A normalised sensing series across four multiplexed channels from a device functionalised with PBASE in DMSO to attach OR22a nanodiscs. Source-drain current was set at $V_{ds} = 100$ mV while gate current was set at $V_g = 0$ V. The concentration of each 20 μL addition of methyl hexanoate in 1% v/v DMSO 1× PBS is indicated above the time of addition. Current data has been despiked and baseline drift removed in both (a) and (b), while a moving median filter has also been applied to the dataset shown in (b).

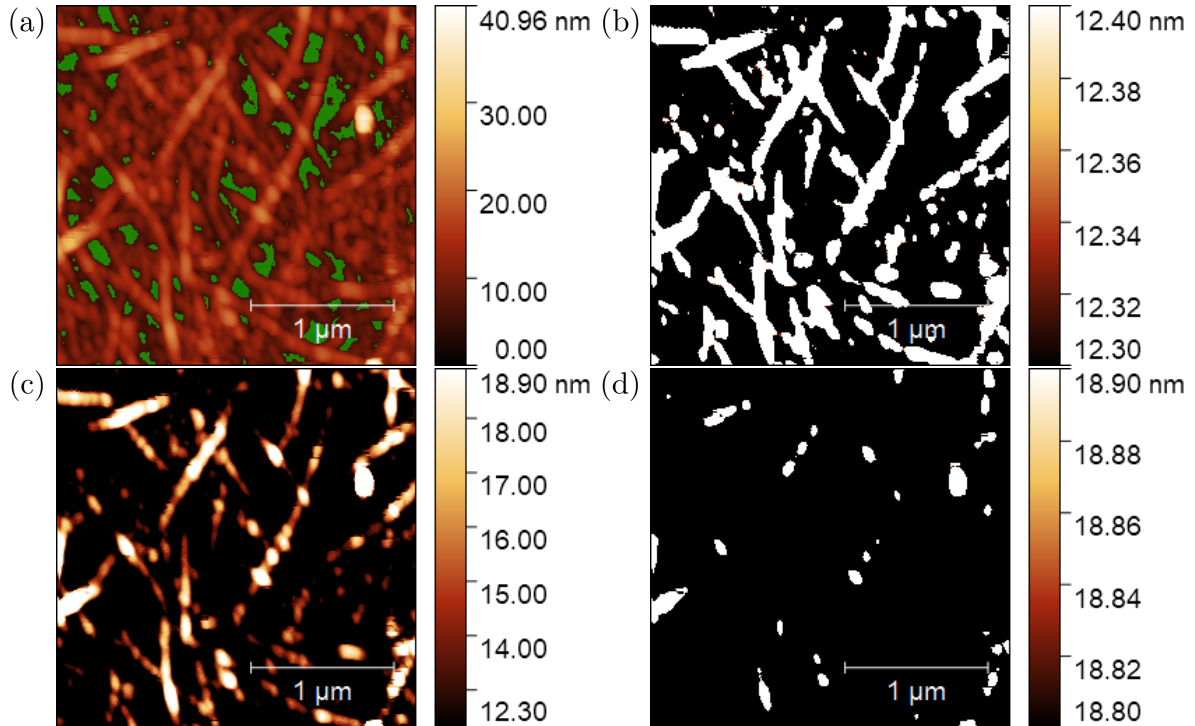


Figure 24: Atomic force microscope images of a carbon nanotube film functionalised with OR22a nanodiscs using PBASE in DMSO. The average substrate height is shown in green in (a). A binary representation of the atomic force microscope image with a threshold height of 12.3 nm is displayed in (b). (c) shows features in the functionalised film across the height range 12.3 – 18.9 nm, while (d) shows another binary representation at 18.8 nm.

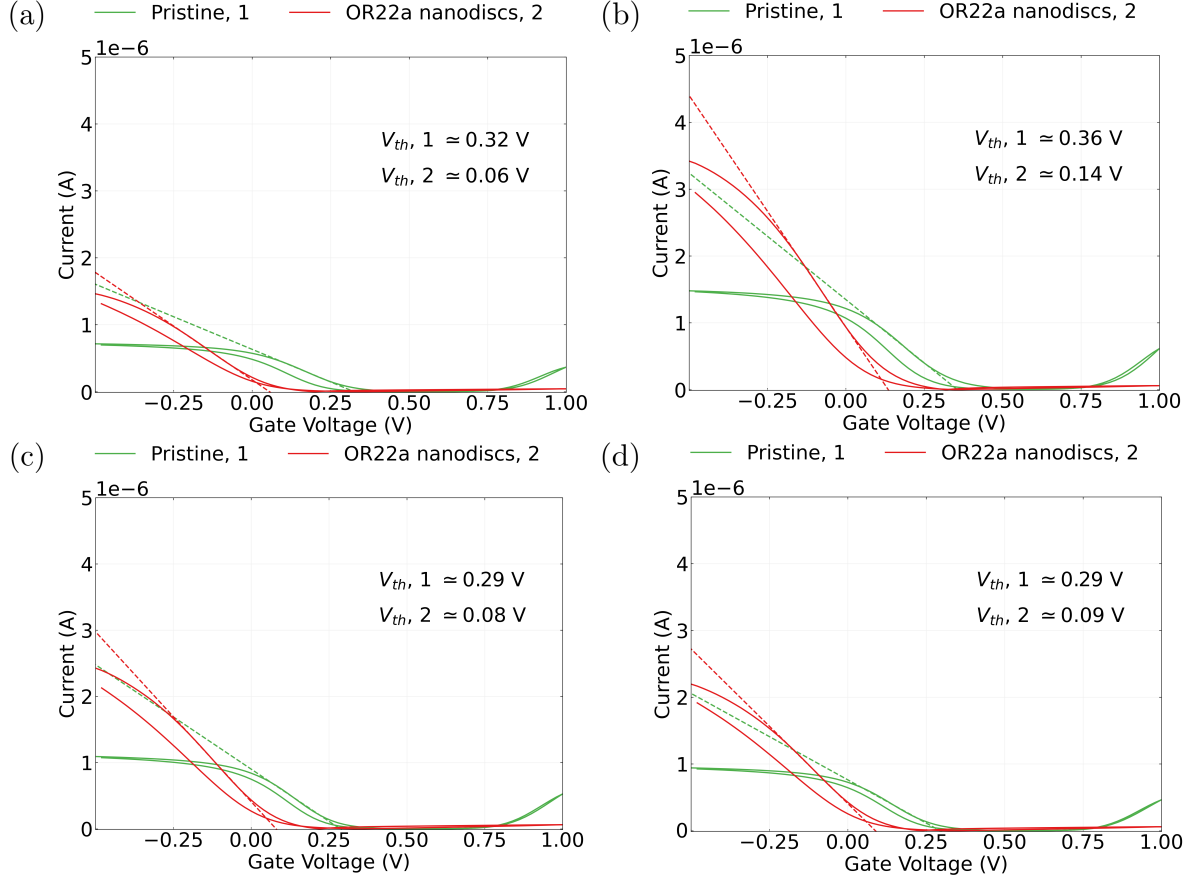


Figure 25: Liquid-gated carbon nanotube network device transfer characteristics before and after OR22a nanodisc functionalisation using PBASE in DMSO. Source-drain current was $V_{ds} = 100$ mV for both the forward and reverse sweep. Each subfigure (a)-(d) corresponds to a different channel of the functionalised device; (a) corresponds to channel 1, (b) corresponds to channel 2, (c) corresponds to channel 3, and (d) corresponds to channel 4. The dashed line shown is tangent to the subthreshold slope of the characteristic curve. The threshold voltage associated with each curve is also shown.

surface, converted to PBASE using carbodiimide (EDC) and succinimide (NHS) reagents. The PBASE is then available to attach to the OR22a nanodiscs as usual. The functionalisation process with PBA was therefore the same as in Section , with the following steps replacing steps 3 – 4:

- A solution of 5 mM PBA (Setareh Biotech) in DMSO was prepared by fully dissolving 7 mg PBASE in 5 mL DMSO by vortex mixing at 1000 rpm.
- The device was left submerged in the 5 mM PBASE in DMSO solution for 1 hour in a parafilm-sealed container.
- A solution of 20 mM EDC and 40 mM NHS in 1× PBS was prepared by dissolving 31 mg EDC and 46 mg NHS in 10 mL 1× PBS.

Note: EDC was thawed under vacuum for 15 minutes in dark conditions before opening.

- The device was rinsed with DMSO for 15 s and 1× PBS for 15 s, then placed into the EDC/NHS solution for 30 minutes.
- The device was then rinsed with 1× PBS for 15s before OR22a nanodisc functionalisation.

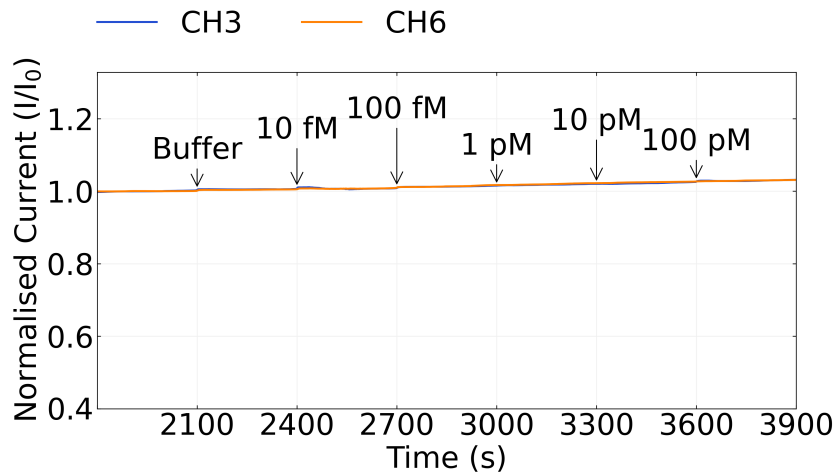


Figure 26: A normalised methyl hexanoate (MeHex) sensing series taken with a OR22a-functionalised carbon nanotube device using PBA with EDC and NHS. Source-drain current was set at $V_{ds} = 100$ mV while gate current was set at $V_g = 0$ V. The concentration of each 20 μ L addition is indicated above the time of addition.

These steps were designed to be broadly similar to those seen in ?@sec-PBA, with an molar excess of NHS relative to EDC to ensure full conversion of the *O*-acylisourea intermediate into PBASE. Normalised, filtered sensing series from two multiplexed channels of the functionalised device are shown in Figure 26. Again, any current response subsequent to additions is positive and <1%. An atomic force microscope image of a film modified in the same manner as the

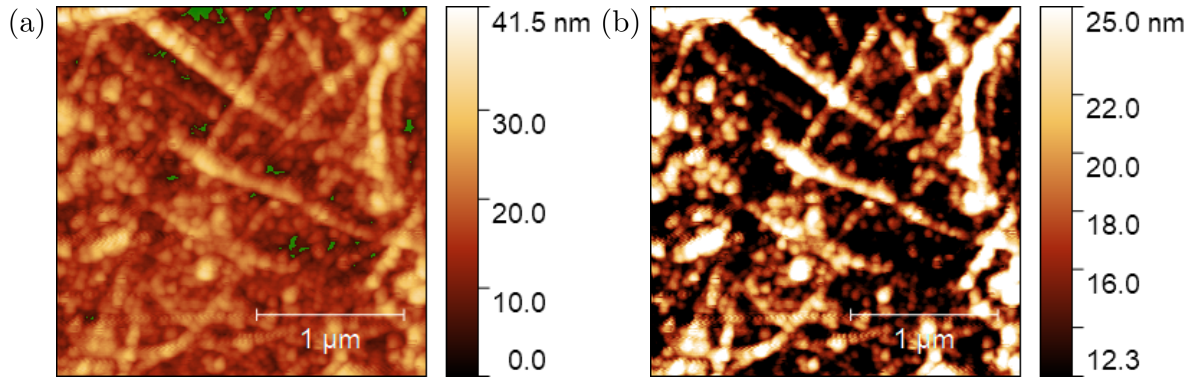


Figure 27: $2.5 \mu\text{m} \times 2.5 \mu\text{m}$ atomic force microscope images of a carbon nanotube film functionalised with OR22a nanodiscs using PBA in DMSO with EDC and NHS. The average substrate height is shown in green in (a), while (b) shows features in the functionalised film across the height range $12.6 - 25.0 \text{ nm}$.

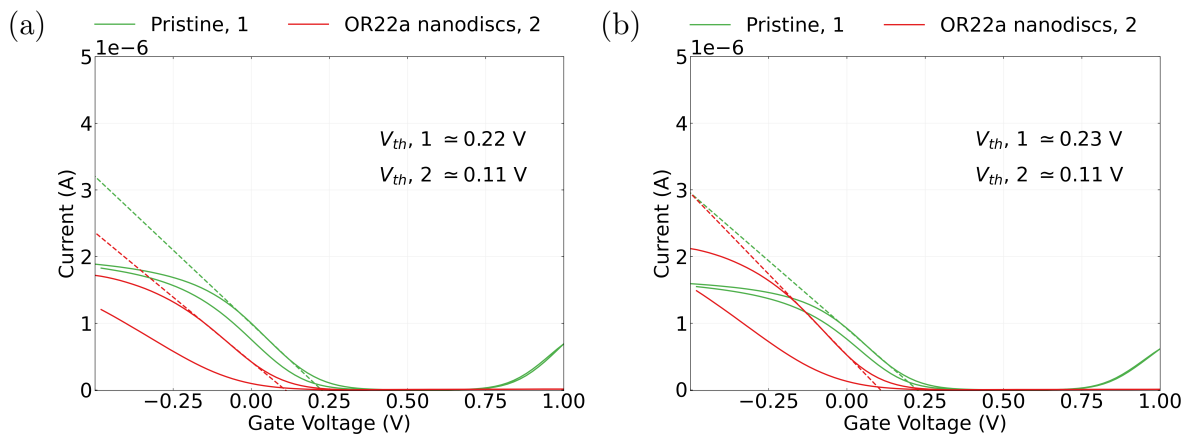


Figure 28: Liquid-gated carbon nanotube network device transfer characteristics before and after OR22a nanodisc functionalisation using PBA in DMSO with EDC and NHS. Source-drain current was $V_{ds} = 100 \text{ mV}$ for both the forward and reverse sweep. Each subfigure corresponds to a different device channel, where (a) is channel 3 and (b) is channel 6. The dashed line shown is tangent to the subthreshold slope of the characteristic curve. The threshold voltage associated with each curve is also shown.

sensing device is shown in Figure 27 (a), with substrate height 3.9 ± 1.5 nm. When a suitable height range above the threshold height 12.6 nm is selected, as in Figure 27 (b), highly clustered nanodisc features with the appearance of pearls on a string are again visible. The transfer characteristics of each channel before and after functionalisation are shown in Figure 28, where an average threshold shift of -0.12 ± 0.01 V is observed. In ?@sec-PBA-characterisation, the threshold shift for PBA attachment in DMSO was -0.15 V. The difference between these two values is not large enough to convincingly conclude whether nanodiscs have attached via PBASE or not. It therefore appears that the problem identified with variability in device behaviour in Section is not resolved by the use of a different solvent or steps to prevent PBASE hydrolysis.

From this elimination process, three possible sources of variability in device performance due to nanoscale surface contamination remain. The first is the hydrocarbonaceous layer that forms due to device exposure to air, which causes channel hydrophobicity. The second is multilayer adhesion of PBASE or PBA on the transducer surface. Finally, photoresist may remain on the device channels, even despite the use of a new method which eliminates photoresist to levels invisible under a fluorescence microscope (?@sec-photoresist-contamination). A further possible source of variability was also identified from the PBASE in DMSO functionalisation, where transfer measurements and AFM imaging both strongly suggested direct attachment of nanodiscs despite the device not functioning as a sensor: attachment of nanodiscs, but with minimal or no attachment of the contained odorant receptors. An altered non-covalent functionalisation method using pyrene-PEG-biotin was therefore developed to eliminate all of the above factors at once and investigate the resulting sensor behaviour. This novel method is trialled in the following section.

iOR Biosensing with Aqueous Functionalisation

Aqueous-Based Functionalisation

A carbon nanotube network field-effect transistor device, fabricated using post-June 2023 methods as described in ?@sec-fabrication, was functionalised with a novel method using OR10a solubilised in surfactant. The odorant receptors were not expressed in a nanodisc format, and were avidin-tagged or “avi-tagged”. This eliminates the possibility of nanodiscs interfering with odorant receptor attachment, though does leave them vulnerable to harsh environmental conditions [@Nath2007; @Bayburt2010]. Upon preparation, the odorant receptors were modified with pyrene-PEG-biotin. The pyrene-PEG-biotin linker attached to the avi-tags on the odorant receptors, as described in ?@sec-NTA-biotin-PEG, allowing them to attach directly from solution to the carbon nanotubes via the attached pyrene linker. This approach meant that no PBASE, PBA or organic solvent was needed in the functionalisation process. To eliminate the remaining possible sources of surface contamination, such as the hydrocarbonaceous coating of nanotubes and residual photoresist, a short oxygen plasma cleaning step was used.

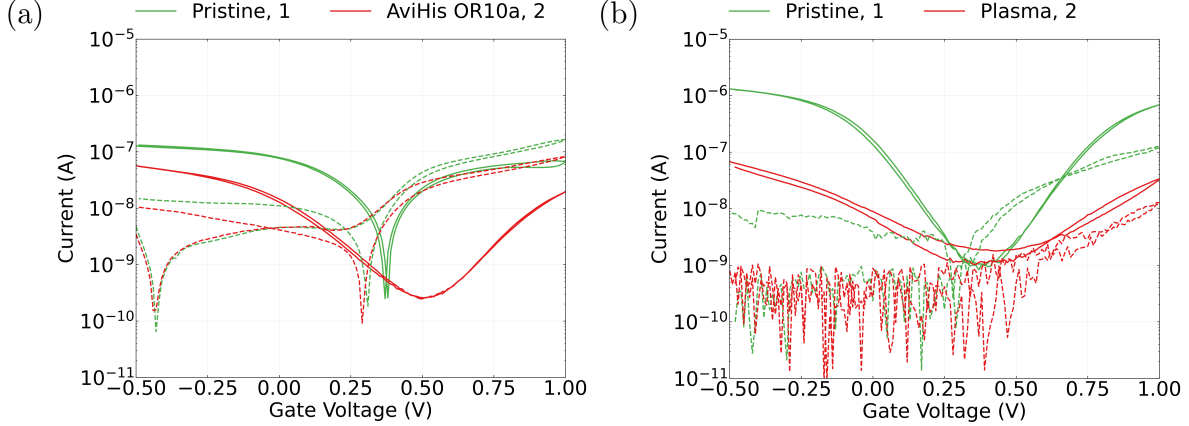


Figure 29: Liquid-gated carbon nanotube network device transfer characteristics on a logarithmic scale before and after modification, where the gate current for each transfer curve is shown with a dashed line. Source-drain current was $V_{ds} = 100$ mV for both the forward and reverse sweep. The change in characteristics from the functionalisation process in this section is shown in (a), while the change resulting from a 5 W plasma clean is shown in (b).

The details of the functionalisation process, loosely based on the non-covalent functionalisation procedure used by Miki *et al.* [Miki2019], are as follows:

1. The device was exposed to UV light for 1 minute, placed in AZ® 326 developer for 3 minutes, then rinsed with acetone, isopropanol and nitrogen dried.
2. The device was vacuum annealed for 1 hour at 150°C.

Note: Steps 1 & 2 were added to either remove or passivate residual photoresist on the channel before functionalisation, see [?@sec-photoresist-contamination](#).

3. 10 μ L surfactant-solubilised avi-tagged OR10a modified with pyrene-PEG-biotin (batch number AviHis-OR10a-001, prepared 12 months earlier) was diluted in 1 mL freshly-prepared 1× PBS.

Note: The full 1 mL was used to flush out the nanodisc vial when preparing the nanodisc solution, with successive additions and subtractions of 50 μ L 1× PBS into and from the vial.

4. Device was treated with a gentle oxygen plasma, ~5 W at 200-300 mTorr, for 15 seconds.

Note: Oxygen plasma was very gentle, with an O_2 flow rate of <10 sccm into the plasma cleaner, to avoid excessive damage to the carbon nanotube network.

5. The device was submerged in the OR10a solution and left covered with parafilm for 15 minutes, then rinsed with 1× PBS for 15 s and thoroughly nitrogen dried.

Figure 29 (a) shows the liquid-gated characteristics of a device channel (channel 2) before and after the functionalisation process with OR10a. The change of characteristics observed can be compared with the change of characteristics seen for a plasma clean only, seen in Figure 29 (b). A significant drop in channel occurs as a result of the plasma cleaning process. This large change in mobility makes it difficult to clearly identify changes in gating specifically due to the presence of the OR10a. The OR10a is not held within a nanodisc format, so the morphology of the functionalised network cannot be compared directly using previous atomic force microscope images. A solvent-deposited carbon nanotube film was prepared separately using OR nanodiscs, where the ORs were attached via their amine group using pyrene-PEG-NHS ester. Pyrene-PEG-NHS ester is very similar to PBASE but contains a PEG chain. Figure 30 shows an atomic force microscope image of the modified film. OR nanodisc aggregates very clearly follow the carbon nanotubes, indicating specific attachment between nanodiscs and carbon nanotubes can be achieved using linker containing pyrene-PEG. The presence of PEG chains may help prevent direct adsorption of proteins onto the carbon nanotubes, improving device quality and therefore sensing behaviour [@Star2003a; @Chen2004].

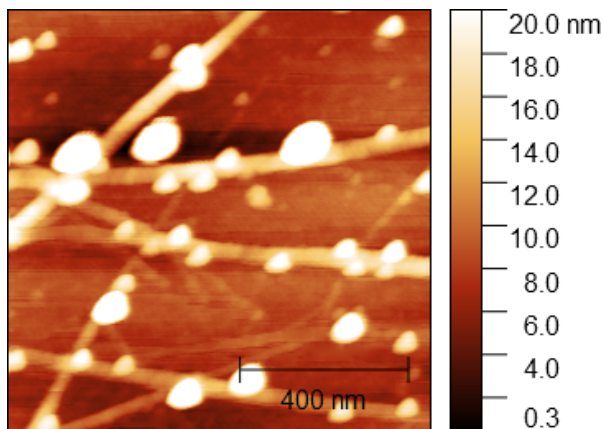


Figure 30: 1 $\mu\text{m} \times 1 \mu\text{m}$ atomic force microscope image of a solvent-deposited carbon nanotube film functionalised with OR nanodiscs using Pyrene-PEG-NHS.

Aqueous Sensing of Methyl Salicylate

The procedure used for sensing methyl salicylate (MeSal) was identical to that used in Section , except using MeSal instead of EtHex. Analyte solutions in 0.5% DMSO/1× PBS solution containing methyl salicylate concentrations at 1 fM, 1 pM, 1 nM and 1 μM were prepared beforehand, The same buffer was used for each dilution, as well as for the well, which contained

80 μ L 0.5% DMSO/1 \times PBS prior to sensing. Sensing measurements were taken using the NI-PXIe system. The full control series plus sensing sequence is shown in Figure 31. Gate current remained negligible across the full sensing procedure, and no responses were seen to buffer additions or subtractions. A linear fit to the baseline drift in the region 1200 – 1800 s, shown in Figure 32 (a), had a gradient of $c_1 = -0.38 \pm 0.01$ pA/s, while an exponential fit to the drift minus the linear fit, shown in Figure 32 (b), had a time constant of 506 ± 12 s. A deviation from the exponential fit similar to that seen for the control series in Section 3 is observed, indicating that $t \ll \tau_i$ does not hold for the drift behaviour and further lending support to the possibility that functionalised devices exhibit characteristic long-term decay behaviour.

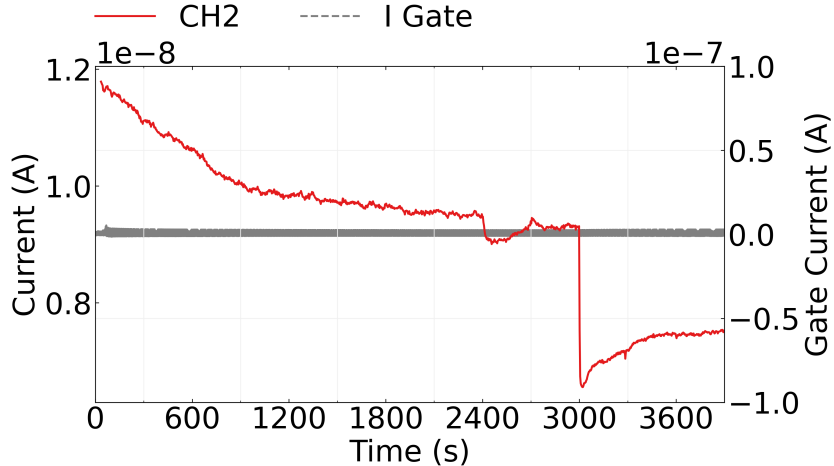


Figure 31: The control series (before 1800 s) and methyl salicylate sensing series (after 1800 s) of the OR10a-functionalised device channel. Source-drain current was set at $V_{ds} = 100$ mV while gate current was set at $V_g = 0$ V. No responses to 0.5% v/v DMSO 1X PBS were seen during the control series, while significant responses to additions of methyl salicylate diluted in 0.5% v/v DMSO 1X PBS were seen at 2400 s and 3000 s.

Cleaned and filtered methyl salicylate sensing data with linear baseline drift removed is shown in Figure 33 (a). The concentration of each 20 μ L methyl salicylate addition is shown above each corresponding addition time. Significant and irreversible current decreases occurred directly after the 1 fM and 1 nM MeSal additions. Figure 33 (b) shows that a $\sim 3\%$ current drop occurred subsequent to the 1 fM addition and a $\sim 23\%$ current drop occurred subsequent to the 1 nM MeSal addition. No negative change in current occurred after the buffer addition, or any of the other three analyte additions. Murugathas *et al.* also observed a similar drop-off in response with increased analyte concentration when sensing with OR10a [Murugathas2019b]. It appears that the OR10a odorant receptors saturate at a low concentration relative to the OR22a odorant receptors tested earlier. Transfer characteristics of the device before and after sensing are shown in Figure 34 (a), showing a threshold shift of -0.07 V.

The device was then rinsed for 15 s in 1 \times PBS after the initial sensing series. The effect of the

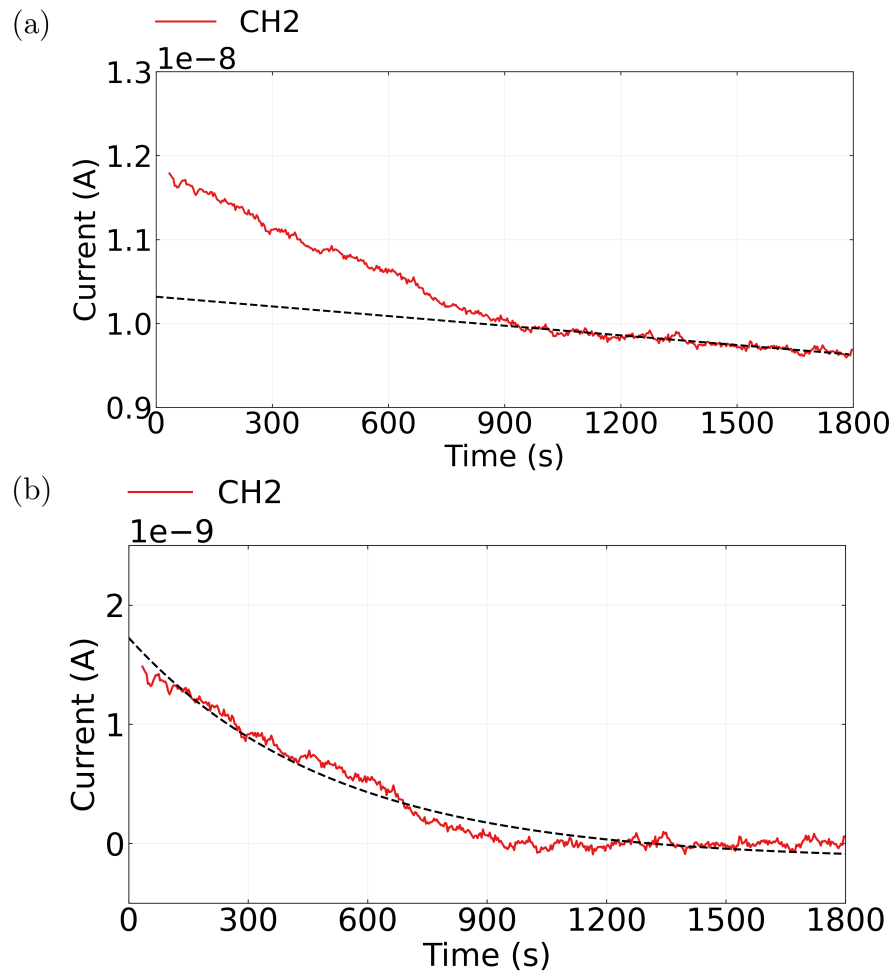


Figure 32: Control series for the OR10a-functionalised device is shown in (a) alongside a linear fit to the control series from 1200 s onwards, where the fit has been extrapolated to 0 s, shown as a black dotted line. The control series with the linear approximation subtracted is shown in (b), fitted with an exponential function shown as a black dotted line.

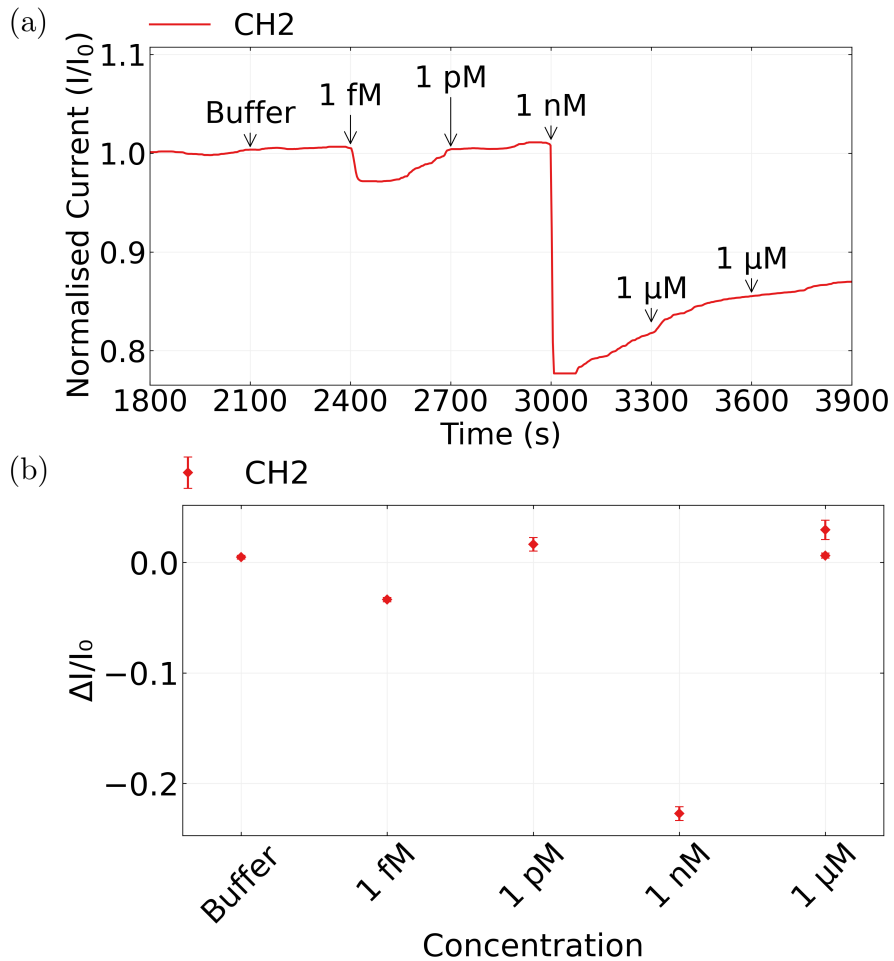


Figure 33: The normalised sensing series for the OR10a-functionalised device is shown in (a), alongside the concentration of each $20 \text{ }\mu\text{L}$ addition. The current data has been despiked, with baseline drift subtracted and a moving median filter applied. The signal data corresponding to the mean difference in current before and after each addition is shown in (b).

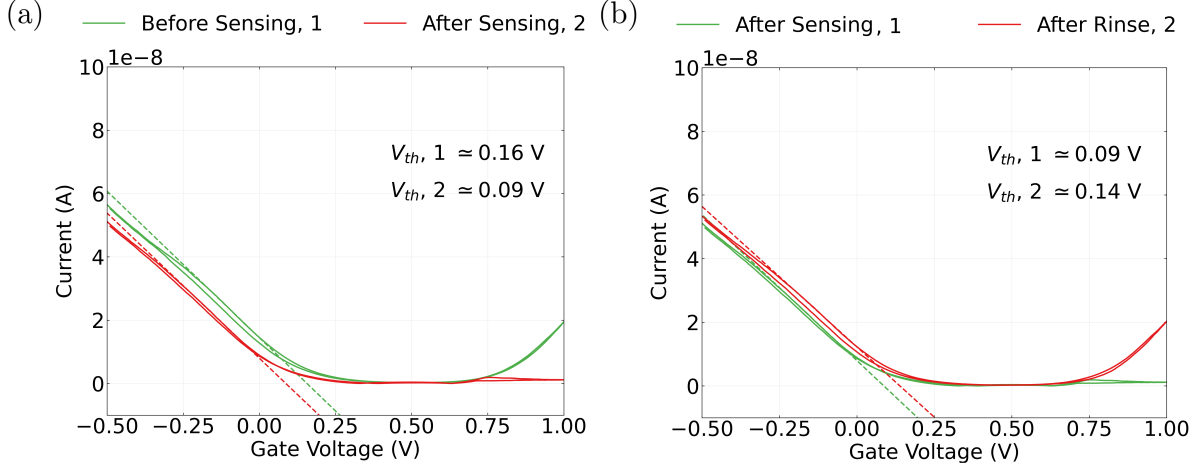


Figure 34: Transfer characteristics of the device after the 1st sensing series, where $V_{ds} = 100$ mV. The transfer characteristics before and after sensing are shown in (a), while (b) shows the channel characteristics before and after being rinsed with 1× PBS.

rinse on the transfer characteristics of the device is illustrated in Figure 34 (b). The rinsing step appears to have largely restored the electrical characteristics of device to their state prior to sensing. It appears the gating effect due to the presence of analyte has been reversed. Assuming that this effect results from structural changes in the odorant receptors, the reversal of threshold shift upon rinsing indicates that without analyte present, the proteins return to their original structure. This implies that the device can be reused as a sensor. Furthermore, as adsorption of solvent leads to gating which is not reversible through rinsing ([?@sec-PBASE-electrical-characterisation](#)), this is also an indication that the responses are not simply due to adsorption of the DMSO present.

A second methyl salicylate sensing series was then performed with the same device, shown in Figure 35 (a). The linear component of baseline drift from 1200 – 1800 s had a gradient of $c_1 = -0.31 \pm 0.01$ pA/s, similar that seen in the previous sensing run. A current response was seen directly after all five analyte additions, shown in Figure 35 (b). Only nanomolar additions of methyl salicylate were used to avoid saturating the proteins and reducing the sensitivity of the sensor. Interestingly, the initial 1 nM analyte addition was similar in size (24%) to the current change resulting from the 1 nM analyte addition in Figure 33 (23%). This result indicates that the size of responses may correspond to the well concentration in a reproducible manner, where there is a specific change in well concentration that gives the largest response. Five successive 20 μ L 1 nM methyl salicylate additions to the 100 μ L buffer in the well results in a well concentration of 500 pM MeSal. Given the steady decrease in analyte response size with successive additions in Figure 35, it appears that the sensor saturates at close to 500 pM, which may explain the lack of response to micromolar additions in Figure 33.

It also appears that the second sensing series resulted in a similar shift in transfer characteristics

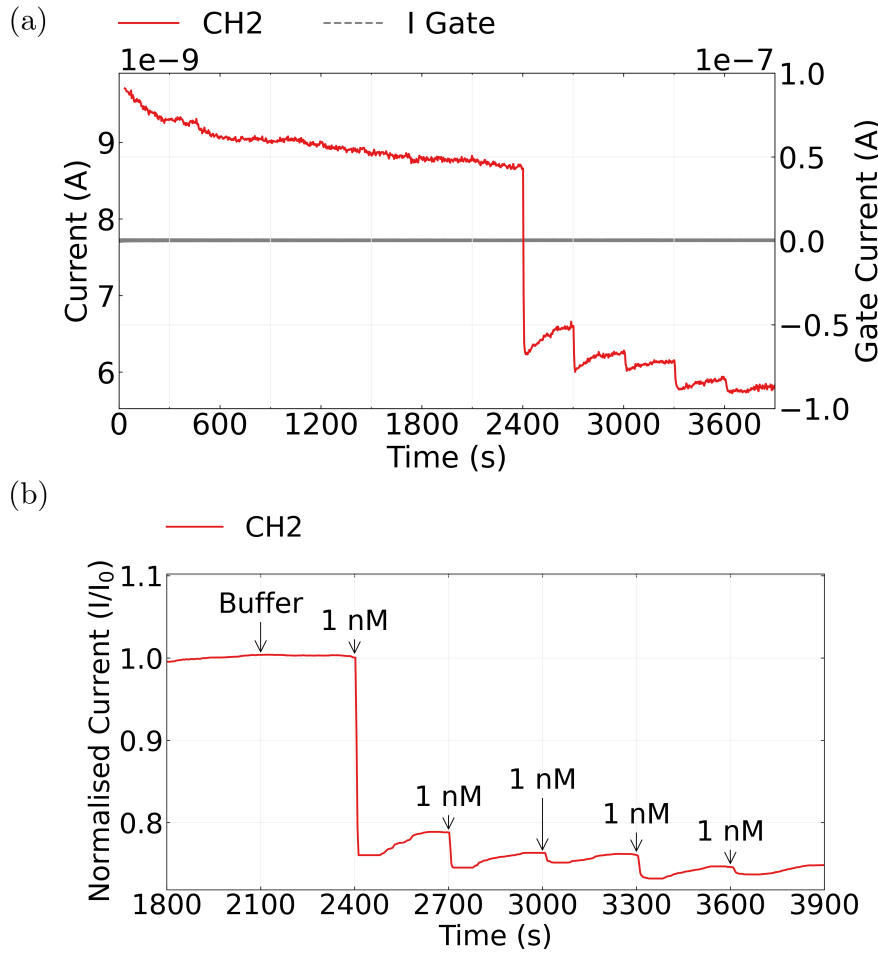


Figure 35: A second methyl salicylate sensing series was performed with the OR10a-functionalised device channel subsequent to rinsing, shown in Figure 35 (a). Source-drain current was set at $V_{ds} = 100$ mV while gate current was set at $V_g = 0$ V. No responses to 0.5% v/v DMSO 1× PBS additions or significant gate current leakage were observed in (a). A clear response is observed after each nanomolar addition of methyl salicylate in (b). The current data in (b) has had a moving median filter applied and linear baseline drift removed.

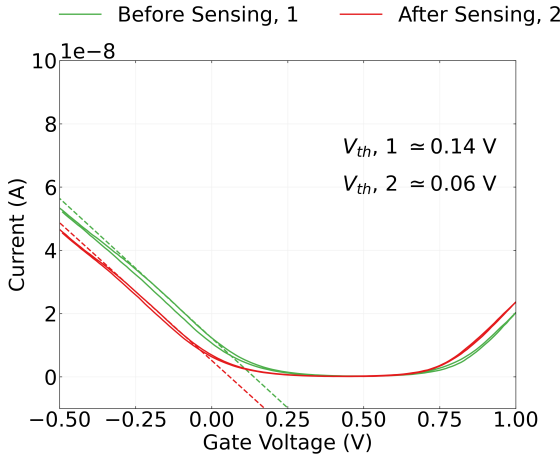


Figure 36: Transfer characteristics of the device directly before and after the 2nd sensing series, where $V_{ds} = 100$ mV.

to that of the first series. Figure 36 shows a shift in threshold voltage of -0.08 V between the transfer characteristics directly before and directly after the nanomolar sensing series. This is another indication that nanomolar additions are enough to cause device saturation. The similarity between Figure 34 (a) and Figure 36 suggests a similar phenomenon has occurred during both sensing series, indicating a odorant receptor-functionalised device can be reused. This is surprising, given the odorant receptors lack a protective membrane. This discussion indicates that the attached odorant receptors can remain viable for at least several hours in room temperature buffer solution, without the need for the nanodisc format.

This method has a number of advantages over the OR nanodisc functionalisation method outlined earlier. The plasma cleaning step eliminates uncertainty stemming from a variety of possible surface coatings on the carbon nanotubes. Using detergent-solubilised odorant receptors removes the possibility that the nanodisks are impeding direct attachment to odorant receptors in the functionalisation procedure. However, it has its own drawbacks. Oxygen plasma cleaning, even at low power, had a invasive effect on the carbon nanotube network. A large drop in mobility resulted from plasma cleaning; for sparser carbon nanotube morphologies, a sizable current drop could leave a device unsuitable for sensing. Since the main advantage of non-covalent functionalisation over covalent functionalisation is its minimal impact on mobility (?@sec-non-covalent-bonding), this approach seems self-contradictory. It appears a less invasive but solvent-free approach should be identified for non-covalent functionalisation [@Ashraf2014], or a well-established covalent approach should instead be used for attaching odorant receptors (?@sec-sensor-types).

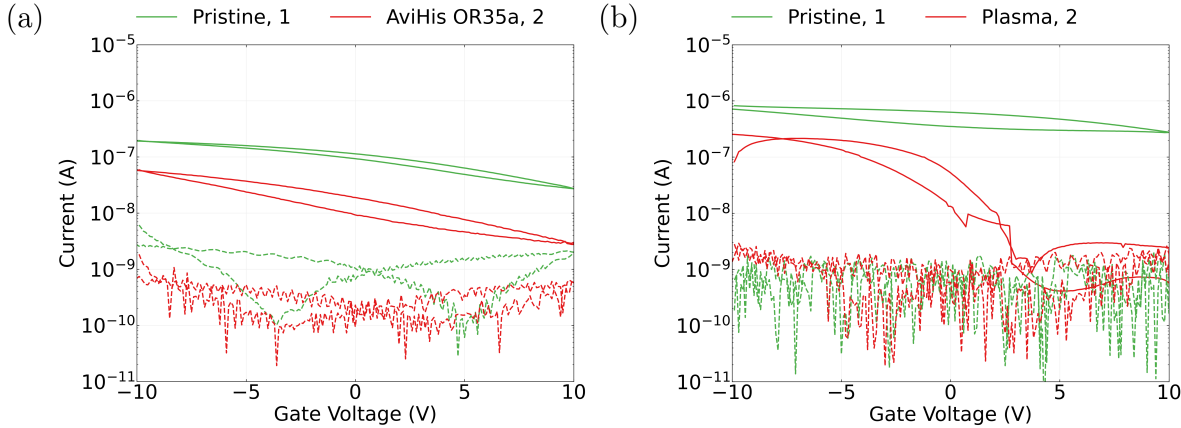


Figure 37: Back-gated carbon nanotube network device transfer characteristics on a logarithmic scale before and after modification, where the gate current for each transfer curve is shown with a dashed line. Source-drain current was $V_{ds} = 100$ mV for each of the forward and reverse sweep. The change in characteristics from avi-tagged OR35a functionalisation is shown in (a), while the change resulting from a 5 W plasma clean is shown in (b).

Vapour Sensing of *trans*-2-hexen-1-al

Despite the drawbacks outlined previously, the functionalisation method in this section was also used to trial vapour phase sensing for the odorant receptor devices. As the vapour pressure of methyl salicylate was too low for reliable vapour system delivery, OR35a (batch number AviHis-OR35a-001, prepared 12 months earlier) was used in the functionalisation process instead of OR10a. OR35a responds to *trans*-2-hexen-1-al (E2Hex) [Murugathas2019b], which is suitable for use in the vapour delivery system. Back-gated transfer characteristics of a OR35a-functionalised before and after functionalisation are shown in Figure 37 (a), alongside characteristics from a device before and after plasma cleaning at 5 W without subsequent functionalisation in Figure 37 (b). As expected, a significant drop in mobility is seen as a result of the plasma cleaning step. Unlike the functionalised device, the device plasma cleaned without functionalisation turns off entirely at $V_g \sim 3$ V, with this difference possibly due to variability in the results of plasma etching for different carbon nanotube devices.

In a similar manner as in ?@sec-pristine-EtHex, the functionalised device was back-gated in the vapour delivery system and a series of exposures to E2Hex was performed. Another pristine device channel was measured during the same sensing series for a baseline comparison. Before each series was performed, the vapour system was purged of vapour, the total dilution flow was set at 200 sccm (nominal) and flow to the PID was set to 150 sccm on the flowmeter. In line with the discussion in ?@sec-vapour-drift, a 2500 s control series was used. The baseline drift is shown in Figure 38, with a backgate of $V_g = 0$ V and a source-drain voltage of $V_{ds} = 100$ mV across the channel during each measurement. During this period, 200 sccm of

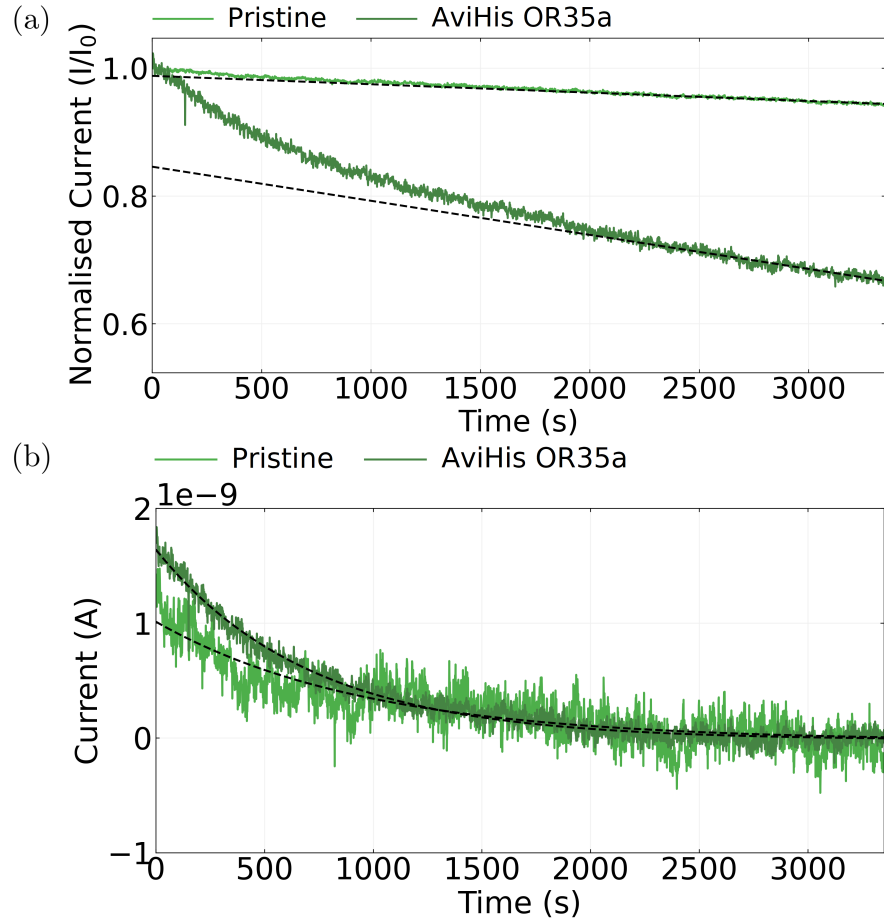


Figure 38: The baseline drift data across the first 2500 s of measurement for both a pristine and OR35a-functionalised device is shown in (a), normalised with respect to the initial datapoint for a clear comparison. A linear fit to the baseline drift data between 2150 – 3350 s is indicated in (a) with a black dashed line. The difference between the raw dataset and linear fit is shown in (b), with an exponential fit to the data indicated with a black dotted line.

nitrogen flow was placed through the device chamber. A linear fit $I = c_1 t + c_2$ was performed on the measurements from each channel between 2150 – 3350 s. For the pristine device, $c_1 = -1.29 \pm 0.01 \text{ pAs}^{-1}$, while for the OR35a-functionalised device, $c_1 = -0.55 \pm 0.01 \text{ pAs}^{-1}$. Figure 38 (b) shows the exponential fit $I = I_0 \exp(-t/\tau)$ to each dataset with linear drift subtracted, where the time constant for the pristine device was $\tau = 963 \pm 25 \text{ s}$ and for the OR35a-functionalised device was $\tau = 704 \pm 4 \text{ s}$.

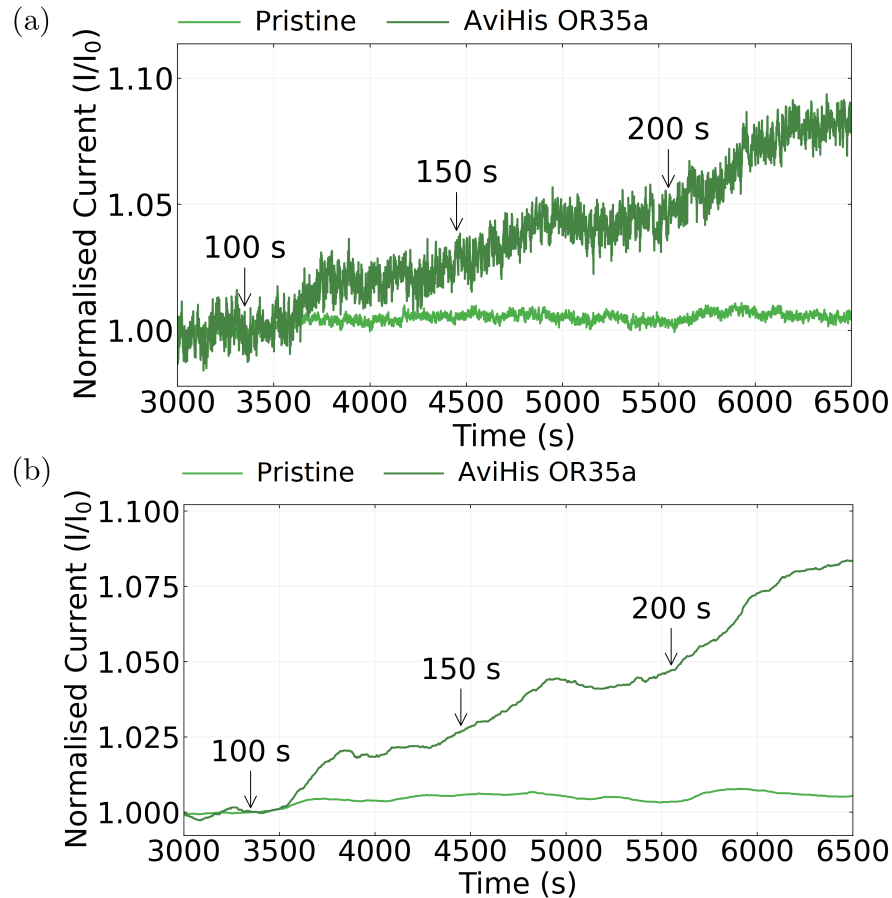


Figure 39: Device channel responses to intervals of flow from the carrier line into the vapour delivery system chamber, showing responses by both the pristine and OR35a-functionalised devices. Intervals begin at 3350 s, 4450 s and 5600 s. The length of each interval is indicated above the corresponding normalised current response to *trans*-2-hexen-1-al (E2Hex) in (a). The dataset after applying a moving median filter is shown in (b).

After the 2500 s control series, each device was exposed to three intervals of *trans*-2-hexen-1-al vapour flow from the carrier line in the same manner. A total of 5 mL of the analyte of interest was present in the analyte bottle before each sensing series. A total flow of 200 sccm was kept

through the chamber at all times. During each interval, 150 sccm of this total flow passed through the carrier line. Except during intervals, no flow was placed through the carrier line. A 1000 s recovery period was used between each interval. The temperature was $20^{\circ}\text{C} \pm 2^{\circ}\text{C}$ during each series. These sensing series, which have been normalised, despiked and corrected for drift, are shown side-by-side in Figure 39 (a), while Figure 39 (b) shows these series after a moving median filter was applied. A larger current change is shown by the functionalised device than the pristine device after each addition. The PID indicated a similar concentration of E2Hex was present in the device chamber with each addition, shown in Figure 40. Note that measurements were taken two days apart; the $\pm 50\%$ variation in chamber concentration reached with each interval is largely due to PID span drift ([?@sec-responses-to-vapour](#)).

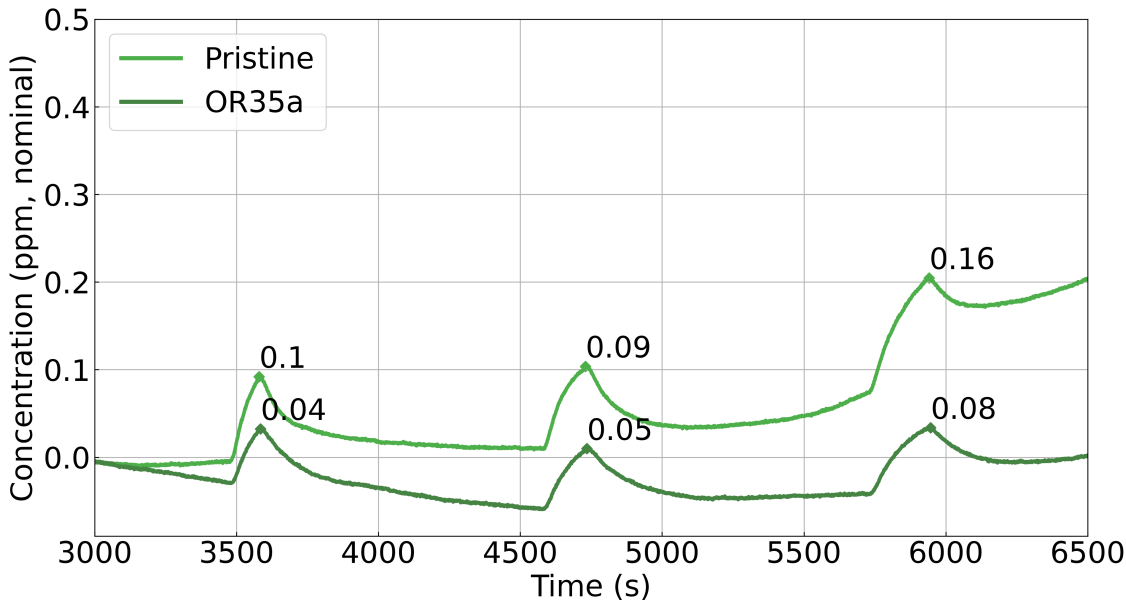


Figure 40: Nominal concentration measurements by the photoionisation detector taken from the device chamber during the vapour sensing series for both pristine and OR35a-functionalised devices. The maximum nominal concentration reached during each interval of carrier flow is indicated above each peak.

The current responses seen are not the sharp, clear responses to analyte of the liquid-gated device seen in Section . Instead, they seem more similar to the responses by bare carbon nanotubes to vapour in [?@sec-vapour-series](#). There are also alternative explanations for the current changes observed in Figure 39 which do not involve specific detection of analyte. The functionalisation may have altered the drift behaviour so that the linear approximation used here for removing baseline drift is no longer useful. It may be useful for future works to incorporate computational approaches to baseline drift compensation if the linear approximation regularly breaks down for functionalised devices [[@Zhang2022](#)]. The breakdown in this approximation has then led to current increases that do not directly correspond to analyte being added. The functionalisation process may also have caused the device to become more

sensitive to changes in vapour concentration, increasing the signal-to-noise ratio of the sensor. Regardless of their origin, the current increases observed cannot fairly be described as clear or convincing sensing responses. A working sensor should exhibit responses more similar to those seen in Section .

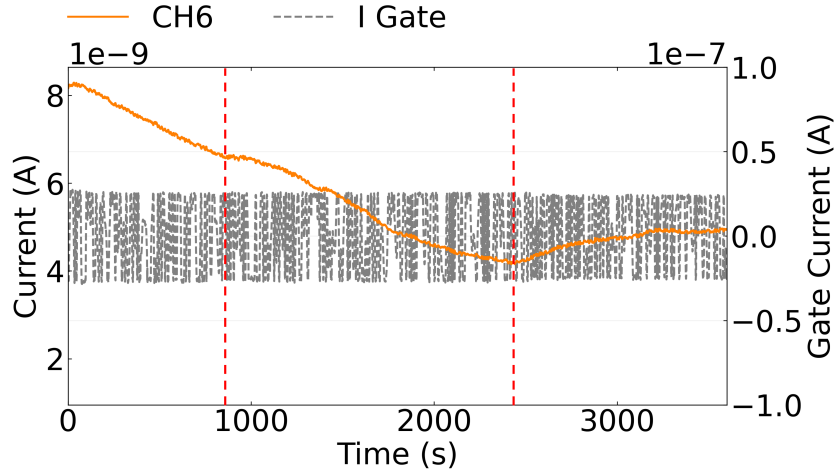


Figure 41: Electrical samples from a carbon nanotube transistor in the vapour delivery system device chamber. Transistor voltages were $V_g = 0$ V and $V_{ds} = 100$ mV. During the measurement, a PDMS well containing 50 μL 0.5% v/v DMSO 1X PBS was present on the device surface. Significant changes in baseline drift behaviour are indicated with red dotted lines.

It may be necessary to ensure the sensing environment is similar to that used for aqueous sensing to achieve reliable sensing. A buffered environment may help to stabilise the unprotected odorant receptors, and so a PDMS well containing 50 μL 0.5% v/v DMSO 1× PBS was attached to the device for vapour sensing. Despite the well being upside-down in the vapour delivery system, the hydrophobicity of the PDMS was sufficient to store the buffer securely. Current sampling over a 1 hour period in this configuration, with 200 sccm constant flow across the surface of the well, is presented in Figure 41. If the well solution was leaking out of the well, the conductive liquid could form a short between the channel electrodes and backgate, prompting a large increase in gate current. However, gate current remains stable across the entire measurement period, indicating the well remains secure. Conversely, fluctuations in drain current became apparent after ~ 800 s, and at ~ 2400 s, the direction of baseline drift was reversed entirely. These undesirable changes appear to result from rapid evaporation of liquid in the well; when the device chamber was opened, only $\sim 10\text{-}20$ μL of buffer was present.

For readily reproducible vapour sensing, therefore, one of two approaches present themselves. The first approach is to identify a covalent attachment mechanism that allows for specific attachment to odorant receptors via a histidine or avidin tag. This approach allows for a protective format like nanodiscs to be used in the sensing setup while eliminating concerns around

unwanted attachment of the protective membrane protein. The weak nature of non-covalent binding lends itself to variable functionalisation quality and poor reproducibility. Non-covalent functionalisation may also be less suitable for use in non-aqueous environments lacking buffer stabilisation [@Li2023]. Conversely, covalent functionalisation of mammalian-OR sensors has been used before for successful vapour sensing of eugenol [@Goldsmith2011]. Alternatively, a similar process to the one investigated here could be used. This non-covalent approach would require the development of a highly reproducible cleaning process, able to remove a variety of organic contaminants from the carbon nanotube surface prior to functionalisation. Furthermore, a liquid capture layer which is both biofriendly and has a low vapour pressure may need to be identified and used. Ideally, this liquid would be miscible with a wide range of substances, but repel PDMS. Further discussion of potential capture layers can be found in ?@sec-future-work-vapour.

Conclusion

A carbon nanotube device was non-covalently functionalised using PBASE in methanol with OR22a nanodiscs and operated as a biosensor in an aqueous environment. Real-time decreases in current level across the sensor channel by up to $\sim 45\%$ were observed in response to analyte additions. Short-term drift behaviour was found to be similar to that of pristine devices, where the fast-decay exponential had a time constant of 590 ± 3 s, but it appears functionalisation may affect long-term baseline drift. Quantitative changes resulting from sensor functionalisation included a device threshold voltage shift of -0.20 ± 0.03 V and a change in network height above the substrate by up to ~ 5 nm, both resulting from the presence of nanodiscs on the network. Additionally, to confirm the presence of odorant receptors on device channels post-functionalisation, ORs were tagged with green fluorescent protein and fluorescence microscope images taken. The functionalised channels showed significantly more green fluorescence than the control. This result indicates protein attachment to the channel is not limited to empty nanodiscs. As far as the author is aware, this is the first time fluorescence has been used to verify the presence of odorant receptors on a carbon nanotube network.

However, the use of the functionalisation procedure with PBASE in methanol and OR22a in nanodiscs was not readily reproducible. A repeat of the functionalisation procedure and sensing procedure across six different device channels showed no decrease in current subsequent to additions ranging from 1 fM to 1 μ M. Further control testing indicated that the successful sensing seen earlier was not spurious, meaning that the lack of reproducibility could be attributed to the functionalisation procedure. Device characterisation showed that although nanodiscs appeared to be present on the channel, with a change in network height above the substrate of up to ~ 20 nm relative to a pristine film, the average threshold shift was -0.06 ± 0.02 V, the same as that of a device functionalised using PBASE in methanol without subsequent exposure to nanodiscs. A control taken without using PBASE also showed nanodiscs present on the channel, with a change in network height above the substrate of up to ~ 10 nm relative to a pristine film, but resulted in a threshold shift of ~ -0.27 V. It therefore appears that

nanodiscs are sometimes being blocked from attaching to the carbon nanotube network in a manner that alters the electrical characteristics of the carbon nanotube network.

Potential confounding variables identified in the functionalisation process included coatings of surfactant, solvent, photoresist, multilayered or hydrolysed PBASE, and the atmospheric long-chain alkanes which cause carbon nanotube hydrophobicity. Several possible confounding variables were individually eliminated by making slight changes to the fabrication and functionalisation of the device. Neither changing the morphology of the carbon nanotube network and using a graphene device led to consistent negative current responses. Furthermore, the average threshold shift for the highly-bundled device after functionalisation was -0.02 ± 0.01 V, indicating a lack of electrical contact between the channel and nanodiscs even without surfactant present. By changing the solvent used for functionalisation from methanol to DMSO, the average threshold shift was -0.22 ± 0.03 V, which demonstrates electrical contact with the nanodiscs. However, no negative current changes were observed subsequent to analyte additions, suggesting multiple confounding factors are at play. To ensure that the hygroscopic DMSO was not hydrolysing the PBASE and preventing odorant receptor attachment, a PBA with EDC/NHS functionalisation method was used. However, the average threshold shift observed was -0.12 ± 0.01 V, similar to the -0.15 V shift seen for attachment of PBA to DMSO without subsequent modification. The confounding factor is therefore not resolved by either changing the solvent or preventing hydrolysis.

The remaining possible sources of surface contamination, including alkane hydrocarbons, multilayer linker and photoresist, were then addressed by making significant changes to the functionalisation procedure. To avoid multilayer coverage, pyrene-PEG-biotin was attached to avi-tagged odorant receptors before functionalisation. To remove hydrocarbons and residual photoresist, the transducer device was gently oxygen plasma cleaned before functionalisation. Furthermore, no nanodiscs were used, to ensure direct attachment of odorant receptors. Although there are also issues with reliable reproducibility of this method due to the plasma cleaning step, when a device was functionalised with OR10a in this manner, device current decreases of up to $\sim 24\%$ were observed in response to methyl salicylate additions. It appears the long-term baseline drift was affected by the functionalisation of the device, where the linear approximation used was relatively weak.

This aqueous functionalisation approach was also used for vapour sensing with OR35a odorant receptors. Clear responses consistent with those seen in an aqueous environment were not observed. The changes in current seen appear more likely to result from a breakdown of the linear approximation of baseline drift for functionalised devices, or from increased non-specific sensitivity of the device post-functionalisation. It was concluded that reproducible vapour sensing would require either a robust covalent functionalisation method which used a protective membrane-like format, or alternatively from using a capture layer to protect non-covalently odorant receptors from the harsh chamber environment. However, it was found 0.5% v/v DMSO 1× PBS could not act as this capture layer due to rapid evaporation of the layer having a significant effect on baseline drift from ~ 800 s onwards. An alternative liquid should therefore be identified which is biofriendly and miscible while having a low vapour

pressure. It should also repel PDMS, to remain contained in the PDMS well upside down in the device chamber. These approaches significantly expand the scope of this work, and are therefore not addressed extensively in this thesis. However, some preliminary work on alternative approaches is discussed in [?@sec-future-work](#).